Journal of Systems Engineering and Electronics
Vol. 34, No. 6, December 2023, pp.1375 – 1396

Two-layer formation-containment fault-tolerant control of fixed-wing UAV swarm for dynamic target tracking

QIN Boyu[1,2], ZHANG Dong[1,2,*], TANG Shuo[1,2], and XU Yang[3]

1. School of Astronautics, Northwestern Polytechnical University, Xi'an 710072, China; 2. Shaanxi Aerospace Flight Vehicle Design Key Laboratory, Xi'an 710072, China; 3. School of Civil Aviation, Northwestern Polytechnical University, Xi'an 710072, China

Abstract: This paper tackles the formation-containment control problem of fixed-wing unmanned aerial vehicle (UAV) swarm with model uncertainties for dynamic target tracking in three-dimensional space in the faulty case of UAVs' actuator and sensor. The fixed-wing UAV swarm under consideration is organized as a "multi-leader-multi-follower" structure, in which only several leaders can obtain the dynamic target information while others only receive the neighbors' information through the communication network. To simultaneously realize the formation, containment, and dynamic target tracking, a two-layer control framework is adopted to decouple the problem into two subproblems: reference trajectory generation and trajectory tracking. In the upper layer, a distributed finite-time estimator (DFTE) is proposed to generate each UAV's reference trajectory in accordance with the control objective. Subsequently, a distributed composite robust fault-tolerant trajectory tracking controller is developed in the lower layer, where a novel adaptive extended super-twisting (AESTW) algorithm with a finite-time extended state observer (FTESO) is involved in solving the robust trajectory tracking control problem under model uncertainties, actuator, and sensor faults. The proposed controller simultaneously guarantees rapidness and enhances the system's robustness with fewer chattering effects. Finally, corresponding simulations are carried out to demonstrate the effectiveness and competitiveness of the proposed two-layer fault-tolerant cooperative control scheme.

Keywords: fixed-wing unmanned aerial vehicle (UAV) swarm, two-layer control, formation-containment, dynamic target tracking.

DOI: 10.23919/JSEE.2023.000153

1. Introduction

With the recent advancements in computing, communication, sensing, and control techniques, the research on unmanned systems in many fields (such as aerospace, marine, and earth science) has become a hot spot and gradually steps into the realistic application [1−4]. In particular, cooperative control of the unmanned aerial vehicle (UAV) swarm system has gained widespread attention by virtue of its potential value in complex and dangerous tasks such as battlefield reconnaissance-attack scenarios, disaster monitoring, and power grid inspection, as well as the efficiency and robustness of task execution [5−9]. As a cooperative control mode that only relies on the local state information of the system, distributed control has been favored by researchers for its advantages of significantly reducing communication costs and effectively enhancing communication robustness. According to the number of leaders in the unmanned systems swarm, distributed control problems can be classified into the following three categories: the leaderless consensus and formation control [10], the "single-leader-single-follower" tracking control [11], and the "multi-leader-multi-follower" containment control [12]. Most cooperative control problems can be abstracted into the combination of the three basic control problems mentioned above.

To incorporate the aforementioned merits of distributed control into UAV swarm, a series of researches focusing on some typical application scenarios have been carried out with various control strategies proposed [13−18]. It is worth mentioning that most results like [14−18] are concerning cooperative control of UAV swarm with either fully distributed or "single-leader-multi-follower" structures. Nevertheless, with respect to cooperative control for UAV swarm with "multi-leader-multi-follower" structure, the attention is still less.

In fact, due to stronger robustness and more diversified task abilities, "multi-leader-multi-follower" structure is more practical in the applications, especially for the swarm consisting of individuals with heterogeneous task capabilities like detection and attack to cooperatively execute different tasks of a target. Recently, some

Manuscript received June 11, 2023.
*Corresponding author.
This work was supported by the National Natural Science Foundation of China (61933010) and the Natural Science Basic Research Plan in Shaanxi Province of China (2023-JC-QN-0733).

researchers have gradually noticed the significance of control for "multi-leader-multi-follower" swarm, and have made some contributions to a coordination scenario, namely "formation-containment" control. However, there still exist limitations mainly reflected in two aspects. First, the agent in the research is usually a theoretical system with highly-abstract mathematical model (like integrator system, high-order linear system) and the proposed controller cannot be directly adopted in the real unmanned systems with more specific and complex dynamics under various uncertainties, faults and disturbances. Second, the swarm is usually desired to keep at fixed points or track a static target. For example, in [19−21], the swarm macroscopic motion was unable to be controlled to track the time-varying reference or maneuvering target.

Up to now, to the best of our knowledge, the attention concerning formation-containment control of fixed-wing UAVs for dynamic target tracking is hitherto rare. It is the primary motivation to develop a practical formation-containment control framework for "multi-leader-multi-follower" fixed-wing UAV swarm system with complex flight dynamics to track dynamic target.

Furthermore, due to the model errors and the possible aging or sticking of mounts of actuators and sensors, uncertainties and faults are the challenges that need to be solved in the fixed-wing UAV control process, which places a high demand on the fault-tolerance and robustness of the UAV controller. This demand becomes more significant when it comes to the UAV swarm system because the negative impacts of the faults on one UAV flight states may be transmitted to others through the communication network. In that way, the negative effects will be amplified with "the Butterfly Effect" induced, and lead to the swarm's performance degradation or even instability [22]. It is therefore meaningful and necessary to propose a control framework of the fixed-wing UAV swarm to simultaneously achieve the formation-containment control for dynamic target tracking and suppress influence of the unknown uncertainties and faults to maintain the performance.

As a key control technique to enhance system robustness and safety against faults and uncertainties, fault-tolerant control (FTC) was widely investigated and applied in many fields [23−25] like electricity generation and wind turbines [26−30]. The application of FTC to cooperative control of multi-UAV/UAV swarm systems, namely fault-tolerant cooperative control (FTCC), became a current hot spot [31−34]. Some FTCC works about the UAV swarm's attitude coordination [35,36], "single-leader-multi-follower" swarm consensus [37], and the UAV formation on the two-dimensional (2D) plane [38] were reported, inspiring to further promote the research on FTCC from both new scenarios and novel approaches. Despite the above outstanding works, how to design the FTCC for the "multi-leader-multi-follower" fixed-wing UAV swarm system to achieve formation-containment control for dynamic target tracking in three-dimensional (3D) space is still a currently unsolved problem. Motivated by the above concerns, this paper intends to address the formation-containment FTC problem of fixed-wing UAV swarm for dynamic target tracking under the model uncertainties, actuator and sensor faults. Compared with the previous literature, this paper contains the following novel features and contributions:

(i) Most existing coordination control of multi-UAV or UAV swarm systems focuses on single-task or dual-task problems (e.g., formation or containment or their combination), which are inappropriate to simultaneously cope with threefold-task problems of formation, containment and dynamic target tracking. Additionally, formation-containment control methods presented in [19−21] are not directly applicable to our case, due to the inherent characteristics of fixed-wing UAV in 3D space.

(ii) In contrast to [5,6,17,39], a novel control-oriented UAV dynamics model in 3D space in the sensor and actuator faulty case is constructed with low-speed aerodynamics and uncertainties of thrust and aerodynamics, which makes the dynamics model more precise to describe the UAV real flight process and more practical for the cooperative controller design.

(iii) In the upper layer, a novel distributed finite-time state estimator (DFTE) is designed for leaders and followers to generate the reference trajectory satisfying the objectives of formation, containment and dynamic target tracking under the circumstance of only several leaders capable of the dynamic target's position and velocity. The designed estimator extends the time adjustable range, and the generated trajectories are much more continuous and smoother compared with [40−42]. The proposed DFTE is therefore more general and practical.

(iv) In the lower layer, a distributed composite robust fault-tolerant trajectory tracking control strategy is developed based on a novel control-oriented UAV dynamics model constructed in 3D space. The nonlinearity induced by model uncertainties and faults are addressed by a novel proposed "adaptive extended super-twisting algorithm" (AESTW) incorporating integral terminal sliding modes and a finite-time extended state observer (FTESO). Compared with the two commonly-used high-order sliding mode control approaches: conventional super-twisting algorithm in [43] and the fast super-twisting algorithm in [44], the proposed AESTW can sufficiently lessen the chattering effects with robustness and

finite-time convergence guaranteed and the signals varies much smoother and continuously, which is meaningful for lower requirements on the signal switching speed of UAV controller in the real application.

2. Preliminaries

2.1 Key notations

Some key notations of the paper are shown in Table 1.

Table 1 Some key notations

Nomenclature	Interpretation
$\boldsymbol{I}_n$	Identity matrix with n dimensions
diag{·}	Diagonal matrix
$\lambda_{\max}(\cdot), \lambda_{\min}(\cdot)$	Maximum and minimum eigenvalues
$\lvert\cdot\rvert, \lVert\cdot\rVert_p$	Absolute value, p-norm
$\mathrm{sgn}(\cdot), \mathrm{sig}^{\alpha}(\cdot)$	Signum function, notation of $\mathrm{sgn}(\cdot)\lvert\cdot\rvert^{\alpha}$
$\otimes$	Kronecker product
$\boldsymbol{L}$	Laplacian matrix
x_i, y_i, z_i	Position coordinates of UAV i
V_i, θ_i, ψ_i	Velocity, path angle, and heading angle of UAV i
T_i, α_i, ϕ_i	Thrust, angle of attack, and banking angle of UAV i
u_{ix}, u_{iy}, u_{iz}	Virtual control input of UAV i
$\boldsymbol{\eta}_{ai}, \boldsymbol{b}_{ai}$	Execution effectiveness, bias of UAV i's actuator
$\boldsymbol{\eta}_{mi}, \boldsymbol{b}_{mi}$	Measurement effectiveness, bias of UAV i's angle sensor
$\boldsymbol{d}_i$	Integrated disturbance and its observed value of UAV i
$\tilde{\boldsymbol{p}}_i, \tilde{\boldsymbol{q}}_i$	Reference position and velocity of UAV i generated by DFTE
$\hat{\boldsymbol{p}}_i, \hat{\boldsymbol{q}}_i, \hat{\boldsymbol{d}}_i$	Position, velocity, and integrated disturbance of UAV i observed by FTESO
$\boldsymbol{s}_i, \varpi_i$	Sliding mode variables

2.2 Fixed-wing UAV model

The dynamics variables are shown in Fig. 1.

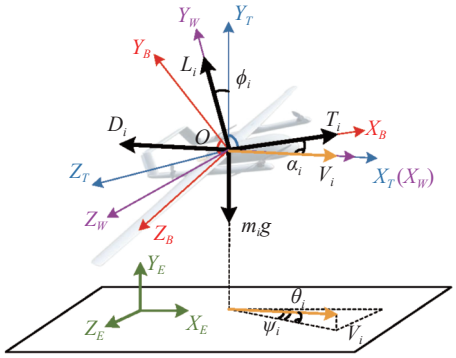

Fig. 1 Coordinate system and dynamics variables

In the following sections of this paper, the model assumes that the autopilot can stabilize the UAV attitude and the slide angle is zero. It is also assumed that the earth is flat and the fuel expenditure is negligible. Under these assumptions, the 3-DOF dynamics model can be described by

$$\begin{cases} \dot{x}_i = V_i \cos\theta_i \cos\psi_i \\ \dot{y}_i = V_i \sin\theta_i \\ \dot{z}_i = -V_i \cos\theta_i \sin\psi_i \end{cases}, \tag{1}$$

$$\begin{cases} \dot{V}_i = \dfrac{(T_i + \Delta T_i)\cos\alpha_i - (D_i + \Delta D_i)}{m_i} - g\sin\theta_i \\ \dot{\theta}_i = \dfrac{[(L_i + \Delta L_i) + (T_i + \Delta T_i)\sin\alpha_i]\cos\phi_i}{m_i V_i} - \dfrac{g\cos\theta_i}{V_i} \\ \dot{\psi}_i = -\dfrac{[(L_i + \Delta L_i) + (T_i + \Delta T_i)\sin\alpha_i]\sin\phi_i}{m_i V_i \cos\theta_i} \end{cases}, \tag{2}$$

where the output is $\boldsymbol{p}_i := [x_i, y_i, z_i]^{\mathrm{T}}$ and the control input is chosen as $\boldsymbol{\mu}_i := [T_i, \alpha_i, \phi_i]^{\mathrm{T}}$. $\boldsymbol{p}_i$ is the position vector of UAV i expressed in the earth coordinate $OX_EY_EZ_E$; g is the gravitational acceleration; m_i is the mass of UAV i; V_i, θ_i, ψ_i are the velocity, path angle, and heading angle, respectively; α_i is the angle of attack; ϕ_i is the bank angle; T_i, L_i, D_i are the nominal thrust, lift, and drag, while ΔT_i, ΔL_i, ΔD_i are the model uncertainties. Note the time-varying external disturbances caused by aerodynamics and thrust model uncertainties as $\boldsymbol{d}_{wi,0} = [d_{wi,x0}, d_{wi,y0}, d_{wi,z0}]^{\mathrm{T}}$, which can be expressed as

$$\begin{cases} d_{wi,x0} = \dfrac{\Delta T_i \cos\alpha_i - \Delta D_i}{m_i} \\ d_{wi,y0} = \dfrac{(\Delta T_i \sin\alpha_i + \Delta L_i)\cos\phi_i}{m_i} \\ d_{wi,z0} = \dfrac{-(\Delta T_i \sin\alpha_i + \Delta L_i)\sin\phi_i}{m_i} \end{cases}. \tag{3}$$

For the low-speed fixed-wing UAV i, the nominal models of lift L_i and drag D_i [45] are respectively

$$\begin{cases} L_i = (C_{L0,i} + C_{Li}^{\alpha}\alpha_i) q_i S_i \\ D_i = \left[C_{D0,i} + \dfrac{l_{ci}}{\pi l_{bi}} (C_{L0,i} + C_{Li}^{\alpha}\alpha_i)^2 \right] q_i S_i \end{cases} \tag{4}$$

where $C_{L0,i}, C_{Li}^{\alpha}$ are the zero-attack-angle lift coefficient and lift derivative. $q_i := \dfrac{1}{2}\rho(V_i - V_{wi})^2$ is dynamic pressure, ρ is the air density, l_{ci} and l_{bi} represent the aerodynamic chord length and span, $V_{wi} = V_{wi,\text{norm}} + V_{wi,\tan}$ is the gust, where $V_{wi,\text{norm}}$ and $V_{wi,\tan}$ represent the normal wind shear and the wind gust turbulence, respectively. The model of the normal wind shear $V_{wi,\text{norm}}$ [46] is

$$V_{wi,\text{norm}} = 0.215 V_{mi} \lg y_i + 0.285 V_{mi} \tag{5}$$

where V_{mi} is the mean wind speed relevant to the height y_i. The wind gust turbulence $V_{mi,\tan}$ is assumed to a Gaussian random variable with zero mean and a standard deviation of $0.09 V_{mi}$.

2.3 Actuator and sensor fault models

In the UAV swarm cooperative control, the actuator and sensor faults may significantly degrade the control performance or even cause system crashes. To improve flight safety, the actuator and sensor faults should be explicitly considered. Inspired by [47,48], the actuator faults consisting of the loss of execution effectiveness and fault bias can be denoted as

$$\boldsymbol{\mu}_i = \boldsymbol{\eta}_{ai}\boldsymbol{\mu}_{i0} + \boldsymbol{b}_{ai},\ \underline{\eta}_{a,ij} \leqslant \eta_{a,ij} \leqslant 1; j = 1,2,3 \tag{6}$$

where $\boldsymbol{\mu}_i$ and $\boldsymbol{\mu}_{i0} = [T_{i0}, \alpha_{i0}, \phi_{i0}]^{\mathrm{T}}$ are the applied and commanded control signal, respectively. $\boldsymbol{\eta}_{ai}$ is the remaining execution effectiveness matrix, where $\boldsymbol{\eta}_{ai} = \text{diag}\{\eta_{a,i1}, \eta_{a,i2}, \eta_{a,i3}\}$, and $\eta_{a,ij}$ is the lower boundary of the execution effectiveness. $\boldsymbol{b}_{ai} = [b_{a,i1}, b_{a,i2}, b_{a,i3}]^{\mathrm{T}}$ is the bounded control bias fault vector. When UAV i is healthy, one has $\eta_{a,i1}, \eta_{a,i2}, \eta_{a,i3} = 1$, $b_{a,i1}, b_{a,i2}, b_{a,i3} = 0$. Note that $\eta_{a,i1}$ and $b_{a,i1}$ represent the impact of engine faults on the thrust; $\eta_{a,i2}$ and $b_{a,i2}$ reflect the effect of pitch channel actuator faults on angle of attack; $\eta_{a,i3}$ and $b_{a,i3}$ are the bank angle variations caused by the effect of roll channel actuator faults.

The measured signals of the track angle and heading angle used by the controller deviate from the true signals by considering factors such as loss of measurement validity and measurement bias error of the angle sensor. The sensor fault model of UAV i is

$$\begin{bmatrix} \theta'_i \\ \psi'_i \end{bmatrix} = \boldsymbol{\eta}_{mi} \begin{bmatrix} \theta_i \\ \psi_i \end{bmatrix} + \boldsymbol{b}_{mi},\ \underline{\eta}_{m,ij} \leqslant \eta_{m,ij} \leqslant 1; j = 1,2 \tag{7}$$

where θ_i and ψ_i represent the real signal of the path angle and heading angle of UAV i, respectively. θ'_i and ψ'_i are denoted as the measured signal of the path angle and heading angle of UAV i. $\boldsymbol{\eta}_{mi} = \text{diag}\{\eta_{m,i1}, \eta_{m,i2}\}$ is the measurement effectiveness matrix, and $\underline{\eta}_{m,ij}$ is the lower boundary of the measurement effectiveness. $\boldsymbol{b}_{mi} = [b_{m,i1}, b_{m,i2}]^{\mathrm{T}}$ is the measurement bias fault vector. $\eta_{m,i1}, b_{m,i1}, \eta_{m,i2}$, and $b_{m,i2}$ reflect the impact of sensor faults on the measurement of the path angle and heading angle of UAV i, respectively.

2.4 Model transformation

In general, the angle of attack α_i of UAV i during the flight is so small that $\cos\alpha_i \approx 1$ and $\sin\alpha_i \approx \alpha_i$, and simultaneously the thrust term $T_i \sin\alpha_i$ can be neglected since it is far smaller than lift L_i [49]. Meanwhile, only the linear terms of drag concerning the angle of attack α_i are retained, and the higher-order terms are treated as perturbations. By substituting (4), (6), and (7) into (2), one can render that

$$\begin{cases} \dot{V}_i = \dfrac{T_{i0} - \left(C_{D0,i} + \dfrac{l_{ci}}{\pi l_{bi}} C_{L0,i}^2 + \dfrac{2 l_{ci}}{\pi l_{bi}} C_{L0,i} C_{Li}^{\alpha} \alpha_{i0} \right) q_i S_i}{m_i} - \\ \qquad g\sin\theta_i + d_{wi,x} \\ \dot{\theta}_i = \dfrac{1}{V_i} \left(\dfrac{C_{Li}^{\alpha}\alpha_{i0} + C_{L0,i}}{m_i} q_i S_i \cos\phi_{i0} - g\cos\theta_i + d_{wi,y} \right) \\ \dot{\psi}_i = -\dfrac{1}{V_i \cos\theta_i} \left(\dfrac{C_{Li}^{\alpha}\alpha_{i0} + C_{L0,i}}{m_i} q_i S_i \sin\phi_{i0} + d_{wi,z} \right) \end{cases}, \tag{8}$$

$$\begin{cases} d_{wi,x} = \left(\dfrac{2 l_{ci}}{\pi l_{bi}} C_{L0,i} C_{Li}^{\alpha} ((1-\eta_{a,i1})\alpha_{i0} - b_{a,i2}) - \right. \\ \qquad \left. \dfrac{2 l_{ci}}{\pi l_{bi}} (C_{Li}^{\alpha})^2 (\alpha_{i0}^2 + (\eta_{a,i1}\alpha_{i0} + b_{a,i1})^2) \right) \cdot \dfrac{1}{m_i} + \\ \qquad (\eta_{a,i1} - 1) T_{i0} + b_{a,i1} + d_{wi,x0} \\ d_{wi,y} = ((C_{Li}^{\alpha}(\eta_{ai,2}\alpha_{i0} + b_{a,i2}) + C_{L0,i}) q_i S_i \cdot \\ \qquad \cos(\eta_{a,i3}\phi_{i0} + b_{a,i3}) - (C_{Li}^{\alpha}\alpha_{i0} + C_{L0,i}) q_i S_i \cdot \cdot \\ \qquad \cos\phi_{i0}) \cdot \dfrac{1}{m_i} + d_{wi,y0} \\ d_{wi,z} = ((C_{Li}^{\alpha}(\eta_{ai,2}\alpha_{i0} + b_{a,i2}) + C_{L0,i}) q_i S_i \cdot \\ \qquad \sin(\eta_{a,i3}\phi_{i0} + b_{a,i3}) - C_{Li}^{\alpha}\alpha_{i0} + C_{L0,i}) \cdot \\ \qquad q_i S_i \sin\phi_{i0}) \cdot \dfrac{1}{m_i} + d_{wi,z0} \end{cases} \tag{9}$$

From (1), (2), and (6)−(9), the control-oriented UAV

model with actuator and sensor faults can be obtained as follows:

$$\begin{cases}\dot{\boldsymbol{p}}_i = \boldsymbol{q}_i \\ \dot{\boldsymbol{q}}_i = \boldsymbol{R}_i(\boldsymbol{R}'_i)^{-1}\boldsymbol{R}_i\boldsymbol{u}_{mi} + \boldsymbol{R}_i\boldsymbol{d}_{wi} + \boldsymbol{g}_y = \boldsymbol{u}_i + \boldsymbol{d}_i\end{cases} \tag{10}$$

where $\boldsymbol{u}_i = [u_{ix}, u_{iy}, u_{iz}]^{\mathrm{T}} = \boldsymbol{R}_i\boldsymbol{u}_{mi} + \boldsymbol{g}_y$ is the virtual control, $\boldsymbol{q}_i = [v_{ix}, v_{iy}, v_{iz}]^{\mathrm{T}}$ is the velocity vector, $\boldsymbol{g}_y := [0, -g, 0]^{\mathrm{T}}$, $\boldsymbol{d}_i = (\boldsymbol{R}_i(\boldsymbol{R}'_i)^{-1} - \boldsymbol{I}_3)\boldsymbol{R}_i\boldsymbol{u}_{mi} + \boldsymbol{R}_i\boldsymbol{d}_{wi}$ is the integrated disturbance, $\boldsymbol{u}_{mi}$ and $\boldsymbol{R}_i$ can be expressed as

$$\begin{cases} u_{mi,1} = \dfrac{1}{m_i}(T_{i0} - (C_{D0,i} + \dfrac{l_{ci}}{\pi l_{bi}}C_{L0,i}^2 + \\ \qquad \dfrac{2l_{ci}}{\pi l_{bi}}C_{L0,i}C_{Li}^{\alpha}\alpha_{i0})q_iS_i) \\ u_{mi,2} = \dfrac{(C_{Li}^{\alpha}\alpha_{i0} + C_{L0,i})q_iS_i\cos\phi_{i0}}{m_i} \\ u_{mi,2} = \dfrac{(C_{Li}^{\alpha}\alpha_{i0} + C_{L0,i})q_iS_i\sin\phi_{i0}}{m_i} \end{cases}, \tag{11}$$

$$\begin{cases} \boldsymbol{R}_i = \begin{bmatrix} \cos\theta_i\cos\psi_i & -\sin\theta_i\cos\psi_i & \sin\psi_i \\ \sin\theta_i & \cos\theta_i & 0 \\ -\cos\theta_i\sin\psi_i & \sin\theta_i\sin\psi_i & \cos\psi_i \end{bmatrix} \\ \boldsymbol{R}'_i = \begin{bmatrix} \cos\theta'_i\cos\psi'_i & -\sin\theta'_i\cos\psi'_i & \sin\psi'_i \\ \sin\theta'_i & \cos\theta'_i & 0 \\ -\cos\theta'_i\sin\psi_i & \sin\theta'_i\sin\psi'_i & \cos\psi'_i \end{bmatrix} \end{cases}. \tag{12}$$

According to (10)−(12), the mathematical relation between the virtual control vector $\boldsymbol{u}_i$ and the real control input vector $\boldsymbol{\mu}_{i0} = [T_{i0}, \alpha_{i0}, \phi_{i0}]^{\mathrm{T}}$ is

$$\begin{cases} T_{i0} = m_i(u_{xi}\cos\theta_i\cos\psi_i + (u_{yi} + g)\sin\theta_i - \\ \qquad u_{zi}\cos\theta_i\sin\psi_i) + (C_{D0,i} + \dfrac{l_c}{\pi l_b}C_{L0,i}^2 + \\ \qquad \dfrac{2l_c}{\pi l_b}C_{L0,i}C_{Li}^{\alpha}\alpha_{i0})q_iS_i \\ \alpha_{i0} = (m_i(u_{xi}\sin\psi_i + u_{zi}\cos\psi_i) - \\ \qquad C_{y0,i}qS\sin\phi_{i0})\cdot\dfrac{1}{C_{yi}^{\alpha}q_iS_i\sin\phi_{i0}} \\ \phi_0 = \arctan((u_{xi}\sin\psi_i + u_{zi}\cos\psi_i)\cdot \\ \qquad \dfrac{1}{(-u_{xi}\sin\theta_i\cos\psi_i + (u_{yi} + g)cos\theta_i} + \\ \qquad u_{zi}\sin\theta_i\sin\psi_i)) \end{cases}. \tag{13}$$

Assumption 1 For the dynamics system as (10), the integrated disturbance $\boldsymbol{d}_i(t)$ is continuously bounded and differentiable. Its derivative $\|\dot{\boldsymbol{d}}_i\|_2 \leqslant d_M$.

Remark 1 Assumption 1 is a common assumption in the research of disturbance-observer based control. In the application, the integrated disturbance caused by many real physical processes meets this assumption. For example, the actuators and sensor efficiency may gradually decrease in a period of time and keep at a constant level at the end, and the bias of actuators and sensors may keep a constant. In these scenarios, the derivatives of disturbances are generally bounded.

2.5 Graph theory

Regarding one target and the UAV swarm containing N_l leader UAVs and N_f follower UAVs, assume that the target and each UAV are the nodes in a directed graph $\mathcal{G} = \{\mathcal{V}, \mathcal{E}, \mathcal{A}\}$, where $\mathcal{V} = \{v_1, v_2, \cdots, v_N\}$ represents the set of nodes, $N = N_l + N_f + 1$ is the total number of nodes. The target is numbered 0, while the number sets of leaders and followers are denoted as $\mathcal{L} = \{1, 2, \cdots, N_l\}$ and $\mathcal{F} = \{N_l + 1, N_l + 2, \cdots, N_l + N_f\}$; $\mathcal{E} \subseteq \{(v_i, v_j) : v_i, v_j \in \mathcal{V}, i \neq j\}$ is denoted as the set of edges, where (v_i, v_j) represents the communication interaction between UAV i and UAV j; $\mathcal{A} = [a^{ij}] \in \mathbf{R}^{N\times N}$ is the adjacency matrix of $\mathcal{G}$; a_{ij} is the communication status, and $a_{ij} = 1$ if $(v_i, v_j) \in \mathcal{E}$, otherwise, $a_{ij} = 0$; the set of neighbor nodes of UAV i is denoted as $\mathcal{N}_i = \{v_j : (v_i, v_j) \in \mathcal{E}\}$. Define the in-degree matrix $\mathcal{D} = \mathrm{diag}\{\deg_{in}(v_i)\}, i = 1, 2, \cdots, N$. Define the Laplacian matrix of $\mathcal{G}$ as $\boldsymbol{L} = \mathcal{D} - \mathcal{A}$. For the directed $\mathcal{G}$, if there exists a directed path from a root node to all other nodes, the graph $\mathcal{G}$ contains a directed spanning tree [50].

Assumption 2 The topology among the target and leader UAVs contains at least one directed spanning tree, the root node of which is the target.

Assumption 3 For each follower UAV, there exists at least a directed path from one of the leader UAVs, the information interactions in both the leader layer and the follower layer are bi-directional.

Remark 2 Assumption 2 and Assumption 3 are common assumptions in the research of formation-containment control. In the application, the hierarchical architecture with multi-leader-multi-follower is a common one when it comes to some scenarios with different agents executing multiple tasks. For example, in the escort missions, the outboard UAVs in the swarm can serve as the leaders to get the target states and guide the whole swarm's movement, while the inner UAVs only need to follow the leaders. By the fore-end process of UAV swarm communication construction, the swarm topology assumptions can be met.

Let Assumption 2 and Assumption 3 hold, the structure division of the Laplacian matrix $\boldsymbol{L} \in \mathbf{R}^{N\times N}$ of the UAV swarm is described as

$$\boldsymbol{L} = \begin{bmatrix} 0 & \boldsymbol{0}_{1\times N_l} & \boldsymbol{0}_{1\times N_f} \\ \boldsymbol{L}_{0l} & \boldsymbol{L}_{ll} & \boldsymbol{0}_{N_l\times N_f} \\ \boldsymbol{0}_{N_l\times 1} & \boldsymbol{L}_{lf} & \boldsymbol{L}_{ff} \end{bmatrix} \tag{14}$$

where $\boldsymbol{L}_{0l} \in \mathbf{R}^{N_l\times 1}$ indicates the leaders' access to the information of the target, $\boldsymbol{L}_{ll} \in \mathbf{R}^{N_l\times N_l}$ represents the interaction among the leaders, $\boldsymbol{L}_{lf} \in \mathbf{R}^{N_f\times N_l}$ represents the communication from the leaders to the followers, and

$\boldsymbol{L}_{lf} \in \mathbf{R}^{N_f \times N_l}$ means the interaction among the followers.

2.6 Control objective

The control objective is to achieve the UAV swarm formation-containment control for the dynamic target tracking in the actuator and sensor faulty case.

For the UAV swarm composed of the leader layer and follower layer, the formation-containment control for tracking the dynamic target is said to be achieved when the following conditions are simultaneously met: (i) the leaders form a desired time-varying formation; (ii) the followers converge into the convex hull of leaders; (iii) the whole swarm tracks the dynamic target. The definitions can be described as follows.

Definition 1 [51] Let X be a set in the real vector space. The convex hull is defined as $\mathrm{Co}(\boldsymbol{x}) = \left\{ \sum_{i=1}^{k} \beta_i x_i | x_i \in X, \beta_i \geqslant 0, \sum_{i=1}^{k} \beta_i = 1 \right\}$.

Definition 2 The UAV swarm system is said to achieve time-varying formation-containment control for tracking the mobile target if for any $i \in \mathcal{F}, j \in \mathcal{L}$ there always exists a set of nonnegative constants $\beta_{i,k}$ satisfying $\sum_{k=1}^{N_l} \beta_{i,k} = 1$ such that

$$\begin{cases} \lim\limits_{t\to\infty} \| \boldsymbol{p}_i(t) - \sum\limits_{k=N_l+1}^{N_f+N_l} \beta_{i,k} \boldsymbol{p}_k(t) \|_2 = 0, \quad i \in \mathcal{F} \\ \lim\limits_{t\to\infty} \| \boldsymbol{p}_j(t) - \boldsymbol{p}_0(t) - \boldsymbol{h}_j(t) \|_2 = 0, \quad j \in \mathcal{L} \end{cases} \tag{15}$$

where $\boldsymbol{p}_0(t)$ represents the position of the mobile target, $\boldsymbol{p}_i(t)$ is the position of UAV i, and $\boldsymbol{h}_i(t)$ is denoted as the leader's desired time-varying formation function, which is piecewise continuously differentiable.

According to the analysis for control objectives of different layers, the control framework is designed as illustrated in Fig. 2.

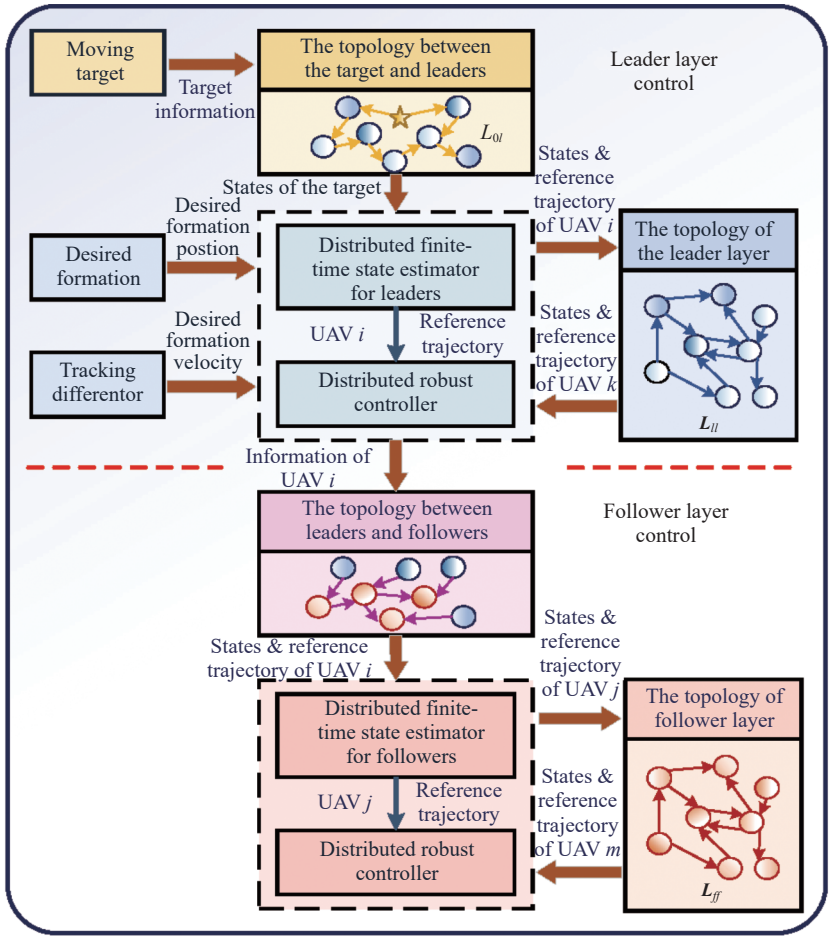

Fig. 2 Hierarchical cooperative control framework

2.7 Lemmas

Lemma 1 [52] Under Assumption 2 and Assumption 3, $\boldsymbol{L}_{ll}$ and $\boldsymbol{L}_{ff}$ are the positive symmetric matrices. Each entry of $-\boldsymbol{L}_{ll}^{-1}\boldsymbol{L}_{0l}$ and $-\boldsymbol{L}_{ff}^{-1}\boldsymbol{L}_{lf}$ is nonnegative, and

each row sum of $-\boldsymbol{L}_{ll}^{-1}\boldsymbol{L}_{0l}$ and $-\boldsymbol{L}_{ff}^{-1}\boldsymbol{L}_{lf}$ is equal to 1.

Lemma 2 [53] Considering the following nonlinear system: $\dot{\boldsymbol{x}} = f(\boldsymbol{x}) + \hat{f}(\boldsymbol{x}), f(0) = 0$, $\boldsymbol{x} \in \mathbf{R}^n$, where $f(\boldsymbol{x})$ is a continuous homogeneous vector of degree $\beta < 0$ with respect to the positive dilation vector $\boldsymbol{r} = [r_1, r_2, \cdots, r_n]$. The function $\hat{f}(\boldsymbol{x})$ satisfies $\hat{f}(0) = 0$. If the equilibrium $\boldsymbol{x} = 0$ is asymptotically stable for $\dot{\boldsymbol{x}} = f(\boldsymbol{x})$, and the following conditions are satisfied: $\lim\limits_{\varepsilon \to 0} \hat{f}_i(\varepsilon^{r_1} x_1, \cdots, \varepsilon^{r_n} x_n)/\varepsilon^{r_i+\beta} = 0$ $(i = 1, 2, \cdots, n), \forall \boldsymbol{x} \neq \boldsymbol{0}$. Then $\boldsymbol{x} = \boldsymbol{0}$ is a locally finite-time equilibrium point. The system is globally finite-time stable if it is both globally asymptotically and locally finite-time stable.

Lemma 3 [53] Consider the following system $\dot{\boldsymbol{x}} = f(\boldsymbol{x}), f(0) = 0, \boldsymbol{x} \in \mathbf{R}^n$. Suppose a positive-definite continuous function $V(\boldsymbol{x}): U \to \mathbf{R}$. If there exists $\dot{V}(\boldsymbol{x}) + cV^{\alpha}(\boldsymbol{x}) \leqslant 0, \boldsymbol{x} \in U_0 \backslash \{0\}$ with the real numbers $c > 0, \alpha \in (0,1)$ in the neighborhood region $U_0 \subset U$, $V(\boldsymbol{x})$ can converge to the origin in a finite time, which satisfies $T \leqslant \dfrac{V^{1-\alpha}(\boldsymbol{x}(0))}{c(1-\alpha)}$.

Lemma 4 [54] With respect to $x_i \in \mathbf{R}$, if $\alpha \in [1, +\infty)$, there exists $\left(\sum\limits_{i=1}^{n} |x_i|\right)^{\alpha} \geqslant \sum\limits_{i=1}^{n} |x_i|^{\alpha} \geqslant n^{1-\alpha}\left(\sum\limits_{i=1}^{n} |x_i|\right)^{\alpha}$; if $\alpha \in (0,1]$, there exists $\left(\sum\limits_{i=1}^{n} |x_i|\right)^{\alpha} \leqslant \sum\limits_{i=1}^{n} |x_i|^{\alpha} \leqslant n^{1-\alpha}\left(\sum\limits_{i=1}^{n} |x_i|\right)^{\alpha}$.

3. Main results

In this section, DFTE is first developed for each UAV to generate the reference trajectories. Then, FTESO is adopted to diagnose the integrated disturbances. In addition, Nonlinear integral terminal sliding mode (NITSM) is designed with the AESTW algorithm proposed to significantly enhance the robustness and effectively weaken the chattering effects. The control architecture is shown in Fig. 3.

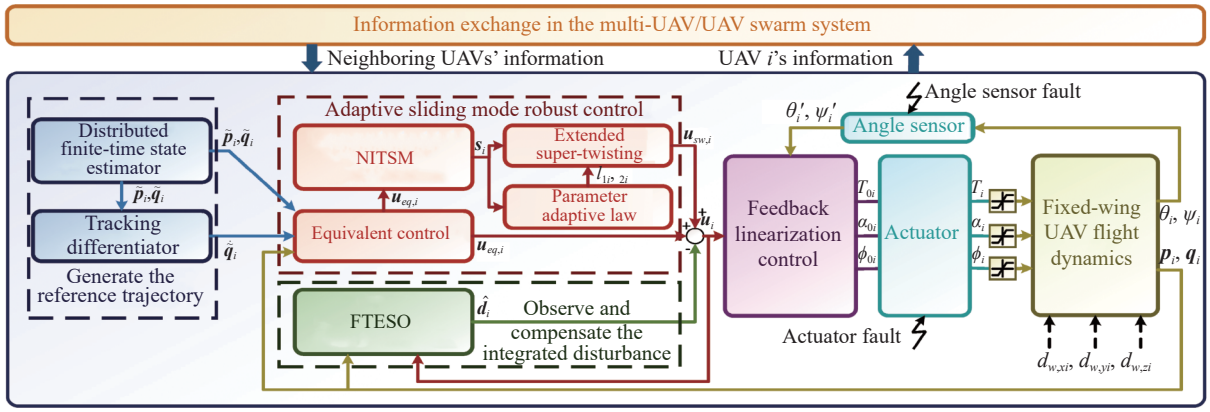

Fig. 3 Structure of the control scheme

3.1 Distributed finite-time estimator

To enable each UAV to online generate the desired trajectory which satisfies the requirements of control objectives, DFTE is designed. Most of the existing distributed state estimators [40−42] adopt sliding mode control (SMC) based on the sign function with discontinuous value, which is sensitive to signal changes and induces the obvious chattering effect.

Considering the above problems, non-smooth functions are introduced to design DFTE to weaken the chattering effect and simultaneously guarantee the robustness and finite-time convergence characteristics.

For the leader UAV i, the distributed finite-time estimator is designed as

$$\begin{cases} \dot{\tilde{\boldsymbol{p}}}_i = \tilde{\boldsymbol{q}}_i - m_1 \mathrm{sig}^{\sigma_0}\left(\sum\limits_{j \in \mathcal{N}_i} a_{ij}((\tilde{\boldsymbol{p}}_i - \boldsymbol{h}_i) - (\tilde{\boldsymbol{p}}_j - \boldsymbol{h}_j))\right) \\ \dot{\tilde{\boldsymbol{q}}}_i = -m_2 \mathrm{sig}^{\sigma_0}\left(\sum\limits_{j \in \mathcal{N}_i} a_{ij}((\tilde{\boldsymbol{q}}_i - \dot{\boldsymbol{h}}_i) - (\tilde{\boldsymbol{q}}_i - \dot{\boldsymbol{h}}_j))\right) \end{cases} \tag{16}$$

where $\tilde{\boldsymbol{p}}_i$ and $\tilde{\boldsymbol{q}}_i$ are respectively the position and velocity estimation of UAV i, and denote the state estimation of the target as $\tilde{\boldsymbol{p}}_0 = \boldsymbol{p}_0$ and $\tilde{\boldsymbol{q}}_0 = \boldsymbol{q}_0$. σ_0, m_1, and m_2 are constants, where $\sigma_0 \in (0,1)$ and $m_1, m_2 > 0$. $\boldsymbol{h}_i$ is the desired time-varying formation function of UAV i from the target, while $\boldsymbol{h}_0 = 0$ for the target.

Assumption 4 The target's position $\boldsymbol{p}_0$, velocity $\boldsymbol{q}_0$ and its derivative $\dot{\boldsymbol{q}}_0$ are bounded, the desired time-varying formation function $\boldsymbol{h}_i$ and its derivatives $\dot{\boldsymbol{h}}_i$ as well as $\ddot{\boldsymbol{h}}_i$ are bounded. Denote $\omega_1, \omega_2, \omega_3$, and ω_4 as the boundness of the norms of $\dot{\boldsymbol{q}}_0, \ddot{\boldsymbol{h}}_i, \dot{\boldsymbol{p}}_0$, and $\dot{\boldsymbol{h}}_i$, respectively.

Remark 3 Assumption 4 is a common assumption in the relevant research. In the real scenario, due to the constraints of the kinematics and maneuvering ability, the target's velocity and the acceleration are always bounded. Also, the desired formation function and its derivative can be always designed as continuous or smooth functions manually based on tasks. Thus, the assumption is reasonable.

Theorem 1 Using the estimators noted by (16), each leader can individually estimate the desired position and velocity in a finite time T_2 for the formation tracking, which can be expressed as

$$\begin{cases}\lim\limits_{t\to T_2}\|\tilde{\boldsymbol{p}}_i(t)-\boldsymbol{p}_0(t)-\boldsymbol{h}_i(t)\|_2\leqslant o_{pL}\\ \lim\limits_{t\to T_1}\|\tilde{\boldsymbol{q}}_i(t)-\boldsymbol{q}_0(t)-\dot{\boldsymbol{h}}_i(t)\|_2\leqslant o_{qL}\end{cases}\tag{17}$$

where o_{pL},o_{qL} are small positive constants, $T_2=T_1+\frac{4}{m_1(1-\sigma_0)}(\frac{\sqrt{\lambda_{\max}(\boldsymbol{L}_{ll})}}{\sqrt{2}\lambda_{\min}(\boldsymbol{L}_{ll})})^{\sigma_0+1}V_{\text{est},2}^{(1-\sigma_0)/2}(T_1)$, $T_1=\frac{4}{m_2(1-\sigma_0)}(\frac{\sqrt{\lambda_{\max}(\boldsymbol{L}_{ll})}}{\sqrt{2}\lambda_{\min}(\boldsymbol{L}_{ll})})^{\sigma_0+1}V_{\text{est},1}^{(1-\sigma_0)/2}(0)$.

Proof Let $\boldsymbol{e}_{pi}=\tilde{\boldsymbol{p}}_i(t)-\boldsymbol{p}_0(t)-\boldsymbol{h}_i(t)$ and $\boldsymbol{e}_{qi}=\tilde{\boldsymbol{q}}_i(t)-\boldsymbol{q}_0(t)-\dot{\boldsymbol{h}}_i(t)$, and note that $\boldsymbol{e}_{pL}=[\boldsymbol{e}_{p1}^{\mathrm{T}},\boldsymbol{e}_{p2}^{\mathrm{T}},\cdots,\boldsymbol{e}_{pN_l}^{\mathrm{T}}]^{\mathrm{T}}$, $\boldsymbol{e}_{qL}=[\boldsymbol{e}_{q1}^{\mathrm{T}},\boldsymbol{e}_{q2}^{\mathrm{T}},\cdots,\boldsymbol{e}_{qN_l}^{\mathrm{T}}]^{\mathrm{T}}$, $\boldsymbol{P}_0=1_{N_l}\otimes\boldsymbol{p}_0$, $\boldsymbol{Q}_0=1_{N_l}\otimes\boldsymbol{q}_0$, $\boldsymbol{h}_L=[\boldsymbol{h}_1^{\mathrm{T}},\boldsymbol{h}_2^{\mathrm{T}},\cdots,\boldsymbol{h}_{N_l}^{\mathrm{T}}]^{\mathrm{T}}$. Define the following Lyapunov candidate:

$$V_{\text{est},1}=\frac{1}{2}\boldsymbol{e}_{qL}^{\mathrm{T}}(\boldsymbol{L}_{ll}\otimes\boldsymbol{I}_3)^{\mathrm{T}}\boldsymbol{e}_{qL}.\tag{18}$$

Substituting (16) into the derivative of (18) yields

$$\begin{aligned}&\dot{V}_{\text{est},1}(t)=\boldsymbol{e}_{qL}^{\mathrm{T}}(\boldsymbol{L}_{ll}\otimes\boldsymbol{I}_3)^{\mathrm{T}}\dot{\boldsymbol{e}}_{qL}=\\&\boldsymbol{e}_{qL}^{\mathrm{T}}(\boldsymbol{L}_{ll}\otimes\boldsymbol{I}_3)^{\mathrm{T}}(-m_2\mathrm{sig}^{\sigma_0}((\boldsymbol{L}_{ll}\otimes\boldsymbol{I}_3)\boldsymbol{e}_{qL})-\dot{\boldsymbol{Q}}_0-\ddot{\boldsymbol{h}}_L)=\\&((\boldsymbol{L}_{ll}\otimes\boldsymbol{I}_3)\boldsymbol{e}_{qL})^{\mathrm{T}}(-m_2\mathrm{sig}^{\sigma_0}((\boldsymbol{L}_{ll}\otimes\boldsymbol{I}_3)\boldsymbol{e}_{qL})+\\&(\boldsymbol{L}_{ll}^{-1}\boldsymbol{L}_{0l}\otimes\boldsymbol{I}_3)(\dot{\boldsymbol{Q}}_0+\ddot{\boldsymbol{h}}_L)).\end{aligned}$$

Considering Lemma 4 and Assumption 4, and $\|\cdot\|_2\leqslant\|\cdot\|_1$, it can be obtained that

$$\begin{aligned}&\dot{V}_{\text{est},1}(t)\leqslant-m_2\|(\boldsymbol{L}_{ll}\otimes\boldsymbol{I}_3)\boldsymbol{e}_{qL}\|_2^{1+\sigma_0}+(\omega_1+\omega_2)\|(\boldsymbol{L}_{ll}\otimes\boldsymbol{I}_3)\boldsymbol{e}_{qL}\|_2\leqslant\\&-(\frac{m_2}{2}\|(\boldsymbol{L}_{ll}\otimes\boldsymbol{I}_3)\boldsymbol{e}_{qL}\|_2^{\sigma_0}-(\omega_1+\omega_2))\cdot\\&\|(\boldsymbol{L}_{ll}\otimes\boldsymbol{I}_3)\boldsymbol{e}_{qL}\|_2-\frac{m_2}{2}\|(\boldsymbol{L}_{ll}\otimes\boldsymbol{I}_3)\boldsymbol{e}_{qL}\|_2^{\sigma_0+1}.\end{aligned}$$

According to the norm properties, when $\|\boldsymbol{e}_{qL}\|_2\geqslant\frac{1}{\|\boldsymbol{L}_{ll}\|_2}(\frac{2(\omega_1+\omega_2)}{m_2})^{1/\sigma_0}$, there exists

$$\begin{aligned}&\dot{V}_{\text{est},1}\leqslant-\frac{m_2}{2}\|(\boldsymbol{L}_{ll}\otimes\boldsymbol{I}_3)\boldsymbol{e}_{qL}\|_2^{\sigma_0+1}\leqslant\\&-\frac{m_2}{2}(\sqrt{\boldsymbol{e}_{qL}^{\mathrm{T}}(\boldsymbol{L}_{ll}\otimes\boldsymbol{I}_3)^2\boldsymbol{e}_{qL}})^{\sigma_0+1}\leqslant\\&-\frac{m_2}{2}(\lambda_{\min}(\boldsymbol{L}_{ll})\|\boldsymbol{e}_{qL}\|_2)^{\sigma_0+1}\leqslant\\&-\frac{m_2}{2}(\frac{\sqrt{2}\lambda_{\min}(\boldsymbol{L}_{ll})}{\sqrt{\lambda_{\max}(\boldsymbol{L}_{ll})}})^{\sigma_0+1}V_{\text{est},1}^{(\sigma_0+1)/2}.\end{aligned}\tag{19}$$

Note that $o_{qL}=\frac{1}{\|\boldsymbol{L}_{ll}\|_2}(\frac{2(\omega_1+\omega_2)}{m_2})^{1/\sigma_0}$. When $m_2>2(\omega_1+\omega_2)/\|\boldsymbol{L}_{ll}\|_2^{\sigma_0}$ and $0<\sigma_0<1$, there exists $2(\omega_1+\omega_2)/(m_2\|\boldsymbol{L}_{ll}\|_2^{\sigma_0})<1$ and $1/\sigma_0>1$, then o_{qL} will be a small positive constant lower than 1. At this time, when $\sigma_0\to0$, there is $1/\sigma_0\to+\infty$, which makes $o_{qL}\to0$.

As a further step, it can be concluded from Lemma 3 that $\lim\limits_{t\to T_1}\|\tilde{\boldsymbol{q}}_i(t)-\boldsymbol{q}_0(t)-\dot{\boldsymbol{h}}_i(t)\|_2\leqslant o_{qL}$ in a finite time $T_1=\frac{4}{m_2(1-\sigma_0)}(\frac{\sqrt{\lambda_{\max}(\boldsymbol{L}_{ll})}}{\sqrt{2}\lambda_{\min}(\boldsymbol{L}_{ll})})^{\sigma_0+1}V_{\text{est},1}^{(1-\sigma_0)/2}(0)$. By adjusting the parameters m_2 and σ_0, it can be obtained that $o_{qL}\approx0$. Then, when $t\geqslant T_1$, consider the Lyapunov function:

$$V_{\text{est},2}=\frac{1}{2}\boldsymbol{e}_{pL}^{\mathrm{T}}(\boldsymbol{L}_{ll}\otimes\boldsymbol{I}_3)^{\mathrm{T}}\boldsymbol{e}_{pL},\tag{20}$$

yielding that

$$\begin{aligned}&\dot{V}_{\text{est},2}=\boldsymbol{e}_{pL}^{\mathrm{T}}(\boldsymbol{L}_{ll}\otimes\boldsymbol{I}_3)^{\mathrm{T}}\dot{\boldsymbol{e}}_{pL}=\\&\boldsymbol{e}_{pL}^{\mathrm{T}}(\boldsymbol{L}_{ll}\otimes\boldsymbol{I}_3)^{\mathrm{T}}(-m_1\mathrm{sig}^{\sigma_0}((\boldsymbol{L}_{ll}\otimes\boldsymbol{I}_3)\boldsymbol{e}_{pL})+\\&(\boldsymbol{L}_{ll}^{-1}\boldsymbol{L}_{0l}\otimes\boldsymbol{I}_3)(\dot{\boldsymbol{P}}_0+\dot{\boldsymbol{h}}_L))\leqslant\\&-(\frac{m_1}{2}\|(\boldsymbol{L}_{ll}\otimes\boldsymbol{I}_3)\boldsymbol{e}_{pL}\|_2^{\sigma_0}-(\omega_3+\omega_4))\cdot\\&\|(\boldsymbol{L}_{ll}\otimes\boldsymbol{I}_3)\boldsymbol{e}_{pL}\|_2-\frac{m_1}{2}\|(\boldsymbol{L}_{ll}\otimes\boldsymbol{I}_3)\boldsymbol{e}_{pL}\|_2^{\sigma_0+1}.\end{aligned}$$

For $\|\boldsymbol{e}_{pL}\|_2\geqslant\frac{1}{\|\boldsymbol{L}_{ll}\|_2}(\frac{2(\omega_3+\omega_4)}{m_1})^{1/\sigma_0}$, there exists

$$\begin{aligned}&\dot{V}_{\text{est},2}\leqslant-\frac{m_1}{2}\|(\boldsymbol{L}_{ll}\otimes\boldsymbol{I}_3)\boldsymbol{e}_{pL}\|_2^{\sigma_0+1}\leqslant\\&-\frac{m_1}{2}\left(\sqrt{\boldsymbol{e}_{pL}^{\mathrm{T}}(\boldsymbol{L}_{ll}\otimes\boldsymbol{I}_3)^2\boldsymbol{e}_{pL}}\right)^{\sigma_0+1}\leqslant\\&-\frac{m_1}{2}(\lambda_{\min}(\boldsymbol{L}_{ll})\|\boldsymbol{e}_{pL}\|_2)^{\sigma_0+1}\leqslant\\&-\frac{m_1}{2}(\frac{\sqrt{2}\lambda_{\min}(\boldsymbol{L}_{ll})}{\sqrt{\lambda_{\max}(\boldsymbol{L}_{ll})}})^{\sigma_0+1}V_{\text{est},2}^{(\sigma_0+1)/2}.\end{aligned}\tag{21}$$

Note that $o_{pL}=\frac{1}{\|\boldsymbol{L}_{ll}\|_2}(\frac{2(\omega_3+\omega_4)}{m_1})^{1/\sigma_0}$. And there is $\lim\limits_{t\to T_2}\|\tilde{\boldsymbol{p}}_i(t)-\boldsymbol{p}_0(t)-\boldsymbol{h}_i(t)\|_2\leqslant o_{pL}$, where $T_2=T_1+\frac{4}{m_1(1-\sigma_0)}(\frac{\sqrt{\lambda_{\max}(\boldsymbol{L}_{ll})}}{\sqrt{2}\lambda_{\min}(\boldsymbol{L}_{ll})})^{\sigma_0+1}V_{\text{est},2}^{(1-\sigma_0)/2}(T_1)$. With the suitable parameters m_1 and σ_0, it can be concluded that $o_{pL}\approx0$.

Therefore, $\hat{p}_i,\hat{\mathrm{v}}_i(i=1,2,\cdots,N_l)$ can be used to replace the position and velocity of the desired formation when $t\geqslant T_2$. □

For follower UAVs, the distributed finite-time estimator is proposed as follows:

$$\begin{cases}\dot{\tilde{\boldsymbol{p}}}_i=\tilde{\boldsymbol{q}}_i-m_3\mathrm{sig}^{\sigma_0}(\sum\limits_{j\in\mathcal{N}_i}a_{ij}(\tilde{p}_i-\tilde{p}_j))\\ \dot{\tilde{q}}_i=-m_4\mathrm{sig}^{\sigma_0}(\sum\limits_{j\in\mathcal{N}_i}a_{ij}(\tilde{q}_i-\tilde{q}_j))\end{cases}\tag{22}$$

where σ_0, m_3, m_4 are constants, and $\sigma_0\in(0,1)$ and $m_3,m_4>0$.

Theorem 2 Using the estimators noted by (22), each follower can individually estimate the desired position and velocity in a finite time T_4 for the containment, which can be expressed as

$$\begin{cases}\lim\limits_{t\to T_4}\|\tilde{\boldsymbol{p}}_i(t)-\boldsymbol{p}_{ci}(t)\|_2\leqslant o_{pF}\\ \lim\limits_{t\to T_3}\|\tilde{\boldsymbol{q}}_i(t)-\boldsymbol{q}_{ci}(t)\|_2\leqslant o_{qF}\end{cases},\ i\in\mathcal{F}\tag{23}$$

where o_{pF}, o_{qF} are small positive constants, $T_4 = T_3 + \frac{4}{m_3(1-\sigma_0)}(\frac{\sqrt{\lambda_{\max}(\boldsymbol{L}_{ff})}}{\sqrt{2}\lambda_{\min}(\boldsymbol{L}_{ff})})^{\sigma_0+1} V_{\text{est},4}^{\frac{1-\sigma_0}{2}}(T_3)$, and $T_3 = \frac{4}{m_4(1-\sigma_0)}(\frac{\sqrt{\lambda_{\max}(\boldsymbol{L}_{ff})}}{\sqrt{2}\lambda_{\min}(\boldsymbol{L}_{ff})})^{\sigma_0+1} V_{\text{est},3}^{\frac{1-\sigma_0}{2}}(0)$. $\boldsymbol{p}_{Ci}$ and $\boldsymbol{q}_{Ci}$ are the ith elements of vectors $\boldsymbol{p}_C = -(\boldsymbol{L}_{ff}^{-1}\boldsymbol{L}_{lf} \otimes \boldsymbol{I}_3)\boldsymbol{p}_L$, $\boldsymbol{q}_C = -(\boldsymbol{L}_{ff}^{-1}\boldsymbol{L}_{lf} \otimes \boldsymbol{I}_3)\boldsymbol{q}_L$, respectively, where $\boldsymbol{p}_L = [\boldsymbol{p}_1^{\mathrm{T}}, \boldsymbol{p}_2^{\mathrm{T}}, \cdots, \boldsymbol{p}_{N_l}^{\mathrm{T}}]^{\mathrm{T}}$ and $\boldsymbol{q}_L = [\boldsymbol{q}_1^{\mathrm{T}}, \boldsymbol{q}_2^{\mathrm{T}}, \cdots, \boldsymbol{q}_{N_l}^{\mathrm{T}}]^{\mathrm{T}}$.

Proof The derivation process is similar to the proof of Theorem 1, so the details will not be presented more here. The reference trajectories of the followers can converge into the convex hull formed by leaders' desired trajectories, i.e., $\tilde{\boldsymbol{p}}_F \to -(\boldsymbol{L}_{ff}^{-1}\boldsymbol{L}_{lf} \otimes \boldsymbol{I}_3)\tilde{\boldsymbol{p}}_L$, $\tilde{\boldsymbol{q}}_F \to -(\boldsymbol{L}_{ff}^{-1}\boldsymbol{L}_{lf} \otimes \boldsymbol{I}_3)\tilde{\boldsymbol{q}}_L$. □

Remark 4 When σ_0 is selected as 0, the function $\text{sig}^{\sigma_0}(\cdot)$ degenerates into the sign function $\text{sgn}(\cdot)$. Correspondingly, the DFTE proposed in this paper is transformed into the distributed sliding-mode state estimator presented in the existing work [40–42]. It can be seen that the existing distributed sliding-mode state estimator is actually a special case of the DFTE in this paper.

3.2 FTESO

The FTESO proposed in [55] is applied to the diagnosis and compensation of the integrated disturbance caused by faults and model uncertainties. Regard the integrated disturbance $\boldsymbol{d}_i$ as the extended state of the system (10), and the observer is described as

$$\begin{cases} \dot{\hat{\boldsymbol{p}}}_i = \hat{\boldsymbol{q}}_i + k_1 \text{sig}^{(\kappa+1)/2}(\boldsymbol{p}_i - \hat{\boldsymbol{p}}_i) \\ \dot{\hat{\boldsymbol{q}}}_i = \hat{\boldsymbol{d}}_i + k_2 \text{sig}^{(\kappa+1)/2}(\boldsymbol{p}_i - \hat{\boldsymbol{p}}_i) + \boldsymbol{u}_i \\ \dot{\hat{\boldsymbol{d}}}_i = k_3 \text{sig}^{\kappa}(\boldsymbol{p}_i - \hat{\boldsymbol{p}}_i) \end{cases} \tag{24}$$

where $\hat{\boldsymbol{p}}_i, \hat{\boldsymbol{q}}_i, \hat{\boldsymbol{d}}_i \in \mathbf{R}^3$ are the estimated states of UAV i, $\kappa \in (0,1)$, $k_1, k_2, k_3 > 0$. If the parameters of the observer satisfy the sufficient conditions presented in [55], FTESO can achieve the precise observation for the integrated disturbance $\boldsymbol{d}_i$.

Remark 5 Here it needs clarifying the FTESO and DFTE. Both of them can be called estimators and observers, but there is a functional difference between them. DFTEs designed in Subsection 3.1 are applied to distributed generating each UAV's reference trajectory based on the neighbor's information for the leaders' formation, the followers' containment, and the whole swarm tracking dynamic target. In contrast, FTESOs in this subsection are used for each UAV to observe and compensate the integrated disturbance, alleviating the negative effects of faults and model uncertainties on UAV swarm flight.

3.3 Distributed adaptive NITSM control

To further enhance the robustness of the control system, NITSM is designed and the AESTW algorithm is simultaneously proposed to track the reference trajectories generated by DFTE so that the system robustness significantly improves while the convergence speed is guaranteed.

The NITSM surface $\boldsymbol{s}_i = [s_{i1}, s_{i2}, s_{i3}]^{\mathrm{T}}$ is designed as

$$\boldsymbol{s}_i(t) = \boldsymbol{q}_i(t) - \boldsymbol{q}_i(0) - \int_0^t \boldsymbol{u}_{eq,i}(\tau)\mathrm{d}\tau \tag{25}$$

where $\boldsymbol{u}_{eq,i} = [u_{eq,i1}, u_{eq,i2}, u_{eq,i3}]^{\mathrm{T}}$ represents the equal input. Apparently, $\boldsymbol{s}_i(0) = \boldsymbol{0}_3$ when $t = 0$, which means that the states of UAV i are located on the sliding mode surface (25) at the initial time. The equal control $\boldsymbol{u}_{eq,i}$ guarantees states of UAV i converge along the sliding mode surface $\boldsymbol{s}_i = \boldsymbol{0}_3$ in a finite time. $\boldsymbol{u}_{eq,i}$ is defined as

$$\begin{aligned} \boldsymbol{u}_{eq,i} = &-l_3 \text{sig}^{\beta_1}(\sum_{j\in\mathcal{N}_i} a_{ij}((\boldsymbol{p}_i - \tilde{\boldsymbol{p}}_i) - (\boldsymbol{p}_j - \tilde{\boldsymbol{p}}_j))) - \\ &l_4 \text{sig}^{\beta_2}(\sum_{j\in\mathcal{N}_i} a_{ij}((\boldsymbol{q}_i - \tilde{\boldsymbol{q}}_i) - (\boldsymbol{q}_j - \tilde{\boldsymbol{q}}_j))) + \dot{\tilde{\boldsymbol{q}}}_i \end{aligned} \tag{26}$$

where $0 < \beta_1 < 1$, $\beta_2 = 2\beta_1/(\beta_1 + 1)$, $l_3, l_4 > 0$. $\dot{\tilde{q}}_i$ can be obtained by the tracking differentiator in [56].

The AESTW algorithm is designed with sliding-mode switching control input $\boldsymbol{u}_{sw,i}$ as

$$\boldsymbol{u}_{sw,i} = -l_1 \text{sig}^{\sigma_1}(\boldsymbol{s}_i) - \int_0^t [l_2 \text{sig}^{\sigma_2}(\boldsymbol{s}_i(\tau))]\mathrm{d}\tau \tag{27}$$

where $0.5 < \sigma_1 < 1$, and $\sigma_2 = 2\sigma_1 - 1$. l_1 and l_2 are adaptive gains, and correspondingly the adaptive law is

$$\dot{l}_1(t) = \begin{cases} w_1 \upsilon_1 (\frac{\sigma_1 - \sigma_2}{2\sigma_1 \upsilon_1})^{\frac{\sigma_1+\sigma_2}{2\sigma_1}}, & |s_{ij}| \geqslant \Delta_s \\ 0, & |s_{ij}| < \Delta_s \end{cases}, \tag{28}$$

$$l_2(t) = \frac{\sigma_1}{2}\varepsilon(l_1(t) + \varepsilon) + \chi, \tag{29}$$

where $\varepsilon > 1/\sigma_1$, $w_1, \upsilon_1, \chi > 0$. $\Delta_s > 0$ and its value is relevant to parameters w_1, υ_1, χ, and the disturbance amplitude δ, which can be adjusted according to the control accuracy.

Taken together, the adaptive NITSM robust control protocol is designed as

$$\boldsymbol{u}_i = \boldsymbol{u}_{eq,i} + \boldsymbol{u}_{sw,i} - \hat{\boldsymbol{d}}_i. \tag{30}$$

Theorem 3 Under the control protocol (30), the UAV swarm (10) with the communication topology G can track the reference trajectories generated by DFTE and achieve the formation-containment control for tracking the dynamic target.

Proof The proof can be divided in two steps: (i) UAV i can approach and then keep on the sliding-mode surface $\boldsymbol{s}_i = \boldsymbol{0}_3$; (ii) When $\boldsymbol{s}_i = \boldsymbol{0}_3$, UAV i can track the estimated states $\tilde{\boldsymbol{p}}_i$ and $\tilde{\boldsymbol{q}}_i$ in a finite time.

For the first step, the derivative of the NITSM (25) is

$$\dot{\boldsymbol{s}}_i = -l_1 \mathrm{sig}^{\sigma_1}(\boldsymbol{s}_i) - \int_0^t (l_2 \mathrm{sig}^{\sigma_2}(\boldsymbol{s}_i(\tau)))\mathrm{d}\tau + \boldsymbol{d}_i - \hat{\boldsymbol{d}}_i. \tag{31}$$

Define $\boldsymbol{\Delta}_i = [\Delta_{i1}, \Delta_{i2}, \Delta_{i3}]^{\mathrm{T}} = \boldsymbol{d}_i - \hat{\boldsymbol{d}}_i$, $\boldsymbol{\varpi}_i = [\varpi_{i1}, \varpi_{i2}, \varpi_{i3}]^{\mathrm{T}} = -\int_0^t (l_2 \mathrm{sig}^{\sigma_2}(\boldsymbol{s}_i(\tau)))\mathrm{d}\tau$, and

$$\begin{cases} \dot{\boldsymbol{s}}_i = -l_1 \mathrm{sig}^{\sigma_1}(\boldsymbol{s}_i) + \boldsymbol{\varpi}_i \\ \dot{\boldsymbol{\varpi}}_i = -l_2 \mathrm{sig}^{\sigma_2}(\boldsymbol{s}_i) + \boldsymbol{\Delta}_i \end{cases}. \tag{32}$$

According to [55], the estimation error of the integrated disturbance $\boldsymbol{d}_i$ is bounded, which yields $\dot{\Delta}_{ij}$ has the boundness as well. Therefore, there exists a positive constant δ satisfying $\|\dot{\Delta}_{ij}\|_2 \leqslant \delta$. Since the control channels (i.e., x, y, and z orientations) are decoupled after feedback linearization, the controller of each channel can be designed individually, indexed by 1, 2, and 3.

Firstly, the finite-time characteristic of AESTW can be proved. Define a vector $\boldsymbol{\xi}_{ij} = [\xi_{ij,1}, \xi_{ij,2}]^{\mathrm{T}} = [\mathrm{sig}^{\sigma_1}(s_{ij}), \varpi_{ij}]^{\mathrm{T}}$, $j \in \{1,2,3\}$. Differentiating $\boldsymbol{\xi}_{ij}$ yields

$$\dot{\boldsymbol{\xi}}_{ij} = |\boldsymbol{\xi}_{ij,1}|^{\frac{\sigma_1 - 1}{\sigma_1}} (\boldsymbol{A}_{ij}\boldsymbol{\xi}_{ij} + \boldsymbol{B}_{ij}\tilde{\Delta}_{ij}) \tag{33}$$

where $\boldsymbol{A}_{ij} = \begin{bmatrix} -l_1\sigma_1 & \sigma_1 \\ -l_2 & 0 \end{bmatrix}$, $\boldsymbol{B}_{ij} = \begin{bmatrix} 0 \\ 1 \end{bmatrix}$, $\tilde{\Delta}_{ij} = |\boldsymbol{\xi}_{ij,1}|^{\frac{1-\sigma_1}{\sigma_1}} \dot{\Delta}_{ij}$. Select a Lyapunov candidate $V_{0,ij} = \boldsymbol{\xi}_{ij}^{\mathrm{T}} \boldsymbol{P}_{ij} \boldsymbol{\xi}_{ij}$, and a positive-definite matrix $\boldsymbol{P}_{ij} = \begin{bmatrix} \frac{\chi}{\sigma_1} + \frac{\varepsilon^2}{2} & -\frac{\varepsilon}{2} \\ -\frac{\varepsilon}{2} & 1 \end{bmatrix}$. The derivative $\dot{V}_{0,ij}$ is

$$\dot{V}_{0,ij} = |\boldsymbol{\xi}_{ij,1}|^{\frac{\sigma_1 - 1}{\sigma_1}} [\boldsymbol{\xi}_{ij}^{\mathrm{T}} (\boldsymbol{A}_{ij}^{\mathrm{T}} \boldsymbol{P}_{ij} + \boldsymbol{P}_{ij} \boldsymbol{A}_{ij}) \boldsymbol{\xi}_{ij} + 2\tilde{\Delta}_{ij} \boldsymbol{B}_{ij}^{\mathrm{T}} \boldsymbol{P}_{ij} \boldsymbol{\xi}_{ij}].$$

Due to $2\tilde{\Delta}_{ij} \boldsymbol{B}_{ij}^{\mathrm{T}} \boldsymbol{P}_{ij} \boldsymbol{\xi}_{ij} \leqslant \boldsymbol{\xi}_{ij}^{\mathrm{T}} \boldsymbol{P}_{ij} \boldsymbol{B}_{ij} \boldsymbol{B}_{ij}^{\mathrm{T}} \boldsymbol{P}_{ij} \boldsymbol{\xi}_{ij} + \tilde{\Delta}_{ij}^2$, $|\tilde{\Delta}_{ij}| = |\boldsymbol{\xi}_{ij,1}|^{\frac{1-\sigma_1}{\sigma_1}} |\dot{\Delta}_{ij}| \leqslant |\boldsymbol{\xi}_{ij,1}|^{\frac{1-\sigma_1}{\sigma_1}} \|\dot{\boldsymbol{\Delta}}_i\| \leqslant |\boldsymbol{\xi}_{ij,1}|^{\frac{1-\sigma_1}{\sigma_1}} \delta$, and supposing $\boldsymbol{C}_{ij} = [1, 0]$, one can obtain

$$\dot{V}_{0,ij} \leqslant |\boldsymbol{\xi}_{ij,1}|^{\frac{\sigma_1 - 1}{\sigma_1}} [\boldsymbol{\xi}_{ij}^{\mathrm{T}} (\boldsymbol{A}_{ij}^{\mathrm{T}} \boldsymbol{P}_{ij} + \boldsymbol{P}_{ij} \boldsymbol{A}_{ij} + \boldsymbol{P}_{ij} \boldsymbol{B}_{ij} \boldsymbol{B}_{ij}^{\mathrm{T}} \boldsymbol{P}_{ij} + \delta^2 \boldsymbol{C}_{ij}^{\mathrm{T}} \boldsymbol{C}_{ij}) \boldsymbol{\xi}_{ij}] + \delta^2 (|\boldsymbol{\xi}_{ij,1}|^{\frac{1-\sigma_1}{\sigma_1}} - |\boldsymbol{\xi}_{ij,1}|^{\frac{3\sigma_1 - 1}{\sigma_1}}).$$

Note $\boldsymbol{A}_{ij}^{\mathrm{T}} \boldsymbol{P}_{ij} + \boldsymbol{P}_{ij} \boldsymbol{A}_{ij} + \boldsymbol{P}_{ij} \boldsymbol{B}_{ij} \boldsymbol{B}_{ij}^{\mathrm{T}} \boldsymbol{P}_{ij} + \delta^2 \boldsymbol{C}_{ij}^{\mathrm{T}} \boldsymbol{C}_{ij} = -\boldsymbol{Q}_{ij}$, so that

$$\dot{V}_{0,ij} \leqslant -|\boldsymbol{\xi}_{ij,1}|^{\frac{\sigma_1 - 1}{\sigma_1}} \boldsymbol{\xi}_{ij}^{\mathrm{T}} \boldsymbol{Q}_{ij} \boldsymbol{\xi}_{ij} + \delta^2 (|\boldsymbol{\xi}_{ij,1}|^{\frac{1-\sigma_1}{\sigma_1}} - |\boldsymbol{\xi}_{ij,1}|^{\frac{3\sigma_1 - 1}{\sigma_1}}) \tag{34}$$

where

$$\boldsymbol{Q}_{ij} = \begin{bmatrix} Q_{ij,11} & Q_{ij,12} \\ Q_{ij,21} & Q_{ij,22} \end{bmatrix},$$

$$\begin{cases} Q_{ij,11} = 2l_1\chi + l_1\sigma_1\varepsilon^2 - l_2\varepsilon - \dfrac{\varepsilon^2}{4} - \delta^2 \\ Q_{ij,12} = -\dfrac{l_1}{2}\sigma_1\varepsilon + l_2 - \chi - \dfrac{\sigma_1}{2}\varepsilon^2 + \dfrac{\varepsilon}{2} \\ Q_{ij,21} = Q_{ij,12} \\ Q_{ij,22} = \sigma_1\varepsilon - 1 \end{cases}.$$

To guarantee $\boldsymbol{Q}_{ij}$ a positive-definite matrix, which implies $-\boldsymbol{Q}_{ij}$ negative-definite, let $l_2 = \dfrac{l_1}{2}\sigma_1\varepsilon + \chi + \dfrac{\sigma_1}{2}\varepsilon^2$, then there exists

$$\begin{cases} Q_{ij,11} = 2l_1\chi + \dfrac{l_1}{2}\sigma_1\varepsilon^2 - \dfrac{\sigma_1}{2}\varepsilon^3 - \dfrac{\varepsilon^2}{4} - \chi\varepsilon - \delta^2 \\ Q_{ij,12} = \dfrac{\varepsilon}{2} \\ Q_{ij,21} = \dfrac{\varepsilon}{2} \\ Q_{ij,22} = \sigma_1\varepsilon - 1 \end{cases}.$$

One can obtain the following inequalities according to the properties of Schur complement:

$$-Q_{ij,22} < 0, \ -Q_{ij,11} + Q_{ij,12}^2 Q_{ij,22}^{-1} < 0.$$

Substitute the expression of $\boldsymbol{Q}_{ij}$ into the above inequalities. And one can render that

$$\begin{cases} \varepsilon > \dfrac{1}{\sigma_1} \\ l_1 > \dfrac{(\frac{\sigma_1}{2}\varepsilon^3 + \frac{\varepsilon^2}{4} + \chi\varepsilon + \delta^2)(\sigma_1\varepsilon - 1) + \frac{\varepsilon^2}{4}}{(2\chi + \frac{\sigma_1}{2}\varepsilon^2)(\sigma_1\varepsilon - 1)} \end{cases}. \tag{35}$$

Substituting $|\boldsymbol{\xi}_{ij,1}| \leqslant \|\boldsymbol{\xi}_{ij}\|_2$ and $\lambda_{\min}(\boldsymbol{Q}_{ij})\|\boldsymbol{\xi}_{ij}\|_2^2 \leqslant \boldsymbol{\xi}_{ij}^{\mathrm{T}} \boldsymbol{Q}_{ij} \boldsymbol{\xi}_{ij} \leqslant \lambda_{\max}(\boldsymbol{Q}_{ij})\|\boldsymbol{\xi}_{ij}\|_2^2$ into (34) yields

$$\dot{V}_{0,ij} \leqslant -\lambda_{\min}(\boldsymbol{Q}_{ij})\|\boldsymbol{\xi}_{ij}\|_2^{\frac{\sigma_1+\sigma_2}{\sigma_1}} + \delta^2(\|\boldsymbol{\xi}_{ij}\|_2^{\frac{1-\sigma_1}{\sigma_1}} + \|\boldsymbol{\xi}_{ij}\|_2^{\frac{\sigma_1+\sigma_2}{\sigma_1}}) = -(\frac{\lambda_{\min}(\boldsymbol{Q}_{ij})}{2} - \delta^2(1 + \|\boldsymbol{\xi}_{ij}\|_2^{-\frac{2\sigma_2}{\sigma_1}}))\|\boldsymbol{\xi}_{ij}\|_2^{\frac{\sigma_1+\sigma_2}{\sigma_1}} - \frac{\lambda_{\min}(\boldsymbol{Q}_{ij})}{2}\|\boldsymbol{\xi}_{ij}\|_2^{\frac{\sigma_1+\sigma_2}{\sigma_1}},$$

when $\left\|\boldsymbol{\xi}_{ij}\right\|_2 > (\dfrac{2\delta^2}{\lambda_{\min}(\boldsymbol{Q}_{ij}) - 2\delta^2})^{\frac{\sigma_1}{2\sigma_2}}$, there exists $\dot{V}_{0,ij} \leqslant -\dfrac{\lambda_{\min}(\boldsymbol{Q}_{ij})}{2}\|\boldsymbol{\xi}_{ij}\|_2^{\frac{\sigma_1+\sigma_2}{\sigma_1}}$. Also, due to $V_{0,ij} \leqslant \lambda_{\max}(\boldsymbol{P}_{ij})\left\|\boldsymbol{\xi}_{ij}\right\|_2^2$, we can get

$$\dot{V}_{0,ij} \leqslant -\vartheta V_{0,ij}^{\frac{\sigma_1+\sigma_2}{2\sigma_1}} \tag{36}$$

where $\vartheta = \dfrac{\lambda_{\min}(\boldsymbol{Q}_{ij})}{2}(\dfrac{1}{\lambda_{\max}(\boldsymbol{P}_{ij})})^{\frac{\sigma_1+\sigma_2}{2\sigma_1}}$. According to Lemma 2 and Lemma 4, (36) indicates that $V_{0,ij}$ is a strong function, which means that the sliding mode variable s_{ij} can converge in a finite time into the following neighborhood:

$$\|\boldsymbol{\xi}_{ij}\|_2 \leqslant \Delta_{s,ij}, \ \Delta_{s,ij} = (\frac{2\delta^2}{\lambda_{\min}(\boldsymbol{Q}_{ij}) - 2\delta^2})^{\frac{\sigma_1}{2\sigma_2}}.$$

Since $\sigma_1 \in (0.5, 1)$, $\dfrac{\sigma_1}{2\sigma_2} \in (0.5, +\infty)$, there exists $\dfrac{2\delta^2}{\lambda_{\min}(\boldsymbol{Q}_{ij}) - 2\delta^2} << 1$ and $\Delta_{s,ij} << 1$ if $\lambda_{\min}(\boldsymbol{Q}_{ij}) >> 4\delta^2$. By adjusting χ and ε, $\lambda_{\min}(\boldsymbol{Q}_{ij})$ can be changed to narrow $\Delta_{s,ij}$.

Then, the convergence of the adaptive law can be

proved. Define the following Lyapunov function:

$$\dot{V}_{ij} = V_{0,ij} + \frac{\sigma_1-\sigma_2}{2\sigma_1\upsilon_1}|l_1-l_1^*|^{\frac{2\sigma_1}{\sigma_1-\sigma_2}} + \frac{\sigma_1-\sigma_2}{2\sigma_1\upsilon_2}|l_2-l_2^*|^{\frac{2\sigma_1}{\sigma_1-\sigma_2}} \tag{37}$$

where $l_1^*, l_2^* > 0$, and $\upsilon_1, \upsilon_2, \chi > 0$. ε is an arbitrary constant. Differentiate the function V_{ij}, and when $\|\boldsymbol{\xi}_{ij}\|_2 \geqslant \Delta_{s,ij}$, there exists:

$$\dot{V}_{ij} \leqslant -\vartheta V_{0,ij}^{\frac{\sigma_1+\sigma_2}{2\sigma_1}} - w_1(\frac{\sigma_1-\sigma_2}{2\sigma_1\upsilon_1})^{\frac{\sigma_1+\sigma_2}{2\sigma_1}}|l_1-l_1^*|^{\frac{\sigma_1+\sigma_2}{\sigma_1-\sigma_2}} - w_2(\frac{\sigma_1-\sigma_2}{2\sigma_1\upsilon_2})^{\frac{\sigma_1+\sigma_2}{2\sigma_1}}|l_2-l_2^*|^{\frac{\sigma_1+\sigma_2}{\sigma_1-\sigma_2}} + \varsigma \tag{38}$$

where $\varsigma = -\frac{\dot{l}_1}{\upsilon_1}|l_1-l_1^*|^{\frac{\sigma_1+\sigma_2}{\sigma_1-\sigma_2}} - \frac{\dot{l}_2}{\upsilon_2}|l_2-l_2^*|^{\frac{\sigma_1+\sigma_2}{\sigma_1-\sigma_2}} + w_1(\frac{\sigma_1-\sigma_2}{2\sigma_1\upsilon_1})^{\frac{\sigma_1+\sigma_2}{2\sigma_1}}|l_1-l_1^*|^{\frac{\sigma_1+\sigma_2}{\sigma_1-\sigma_2}} + w_2(\frac{\sigma_1-\sigma_2}{2\sigma_1\upsilon_2})^{\frac{\sigma_1+\sigma_2}{2\sigma_1}}|l_2-l_2^*|^{\frac{\sigma_1+\sigma_2}{\sigma_1-\sigma_2}}$. When $\sigma_1 \in (0.5, 1)$, there exists $\frac{2\sigma_1}{\sigma_1+\sigma_2} \in (1,2)$. Based on Lemma 4, one can gain

$$\begin{aligned}\dot{V}_{ij} &\leqslant -\min\{\vartheta, w_1, w_2\}(V_{0,ij} + \frac{\sigma_1-\sigma_2}{2\sigma_1\upsilon_1}|l_1-l_1^*|^{\frac{2\sigma_1}{\sigma_1-\sigma_2}} + \\ &\quad \frac{\sigma_1-\sigma_2}{2\sigma_1\upsilon_2}|l_2-l_2^*|^{\frac{2\sigma_1}{\sigma_1-\sigma_2}})^{\frac{\sigma_1+\sigma_2}{2\sigma_1}} + \varsigma = \\ &\quad -\min\{\vartheta, w_1, w_2\}V_{ij}^{\frac{\sigma_1+\sigma_2}{2\sigma_1}} + \varsigma.\end{aligned}$$

To guarantee the property of the finite-time convergence, supposing $\varsigma = 0$ yields

$$\begin{cases}\dot{l}_1 = w_1\upsilon_1(\frac{\sigma_1-\sigma_2}{2\sigma_1\upsilon_1})^{\frac{\sigma_1+\sigma_2}{2\sigma_1}} \\ \dot{l}_2 = w_2\upsilon_2(\frac{\sigma_1-\sigma_2}{2\sigma_1\upsilon_2})^{\frac{\sigma_1+\sigma_2}{2\sigma_1}}\end{cases}. \tag{39}$$

Fix $\frac{2w_2}{\sigma_1 w_1}(\frac{\upsilon_2}{\upsilon_1})^{\frac{\sigma_1-\sigma_2}{2\sigma_1}} = \varepsilon$ and one can obtain $\dot{l}_2 = \frac{\sigma_1}{2}\varepsilon\dot{l}_1$, which is consistent with (28). Overall, the finite-time convergence can be achieved.

The second step is to present the proof of the convergence of the system when $\boldsymbol{s}_i, \dot{\boldsymbol{s}}_i \approx 0$. Under the equal control input (26), there exist

$$\begin{cases}\dot{\boldsymbol{p}}_L = \boldsymbol{q}_L \\ \dot{\boldsymbol{q}}_L = -l_3\mathrm{sig}^{\beta_1}((\boldsymbol{L}_{ll}\otimes\boldsymbol{I}_3)(\boldsymbol{p}_L-\tilde{\boldsymbol{p}}_L)) - \\ \qquad l_4\mathrm{sig}^{\beta_2}((\boldsymbol{L}_{ll}\otimes\boldsymbol{I}_3)(\boldsymbol{q}_L-\tilde{\boldsymbol{q}}_L)) + \dot{\tilde{\boldsymbol{q}}}_L \\ \dot{\boldsymbol{p}}_F = \boldsymbol{q}_F \\ \dot{\boldsymbol{q}}_F = \dot{\tilde{\boldsymbol{q}}}_F - l_3\mathrm{sig}^{\beta_1}((\boldsymbol{L}_{lf}\otimes\boldsymbol{I}_3)(\boldsymbol{p}_L-\tilde{\boldsymbol{p}}_L) + \\ \qquad (\boldsymbol{L}_{ff}\otimes\boldsymbol{I}_3)(\boldsymbol{p}_F-\tilde{\boldsymbol{p}}_F)) - \\ \qquad l_4\mathrm{sig}^{\beta_2}((\boldsymbol{L}_{lf}\otimes\boldsymbol{I}_3)(\boldsymbol{q}_L-\tilde{\boldsymbol{q}}_L) + \\ \qquad (\boldsymbol{L}_{ff}\otimes\boldsymbol{I}_3)(\boldsymbol{q}_F-\tilde{\boldsymbol{q}}_F))\end{cases}. \tag{40}$$

It needs to be shown that the UAV swarm system described in (39) can achieve the desired formation for the leader UAVs the containment for the follower UAVs.

To proceed, firstly for the leader layer, supposing $\bar{\boldsymbol{p}}_L = \boldsymbol{p}_L - \tilde{\boldsymbol{p}}_L$ and $\bar{\boldsymbol{q}}_L = \boldsymbol{q}_L - \tilde{\boldsymbol{q}}_L$ yields:

$$\begin{cases}\dot{\bar{\boldsymbol{p}}}_L = \bar{\boldsymbol{q}}_L + m_1\mathrm{sig}^{\sigma_0}((\boldsymbol{L}_{0l}\otimes\boldsymbol{I}_3)\boldsymbol{p}_0 + \\ \qquad (\boldsymbol{L}_{ll}\otimes\boldsymbol{I}_3)(\tilde{\boldsymbol{p}}_L-\boldsymbol{h}_L)) \\ \dot{\bar{\boldsymbol{q}}}_L = -l_3\mathrm{sig}^{\beta_1}((\boldsymbol{L}_{ll}\otimes\boldsymbol{I}_3)\bar{\boldsymbol{p}}_L) - \\ \qquad l_4\mathrm{sig}^{\beta_2}((\boldsymbol{L}_{ll}\otimes\boldsymbol{I}_3)\bar{\boldsymbol{q}}_L)\end{cases}.$$

According to Lemma 1, one can obtain $\dot{\bar{\boldsymbol{p}}}_L = \bar{\boldsymbol{q}}_L + m_1\mathrm{sig}^{\sigma_0}((\boldsymbol{L}_{ll}\otimes\mathrm{I}_3)((\tilde{\boldsymbol{p}}_L-\boldsymbol{h}_L)-(1_{N_l}\otimes\boldsymbol{p}_0)))$. From the DFTE (16), $\tilde{\boldsymbol{p}}_i \to \boldsymbol{p}_0 + \boldsymbol{h}_i$ $(i \in \mathcal{L})$. Given that each eigen value of the matrix $\boldsymbol{L}_{ll}$ is positive, $m_1\mathrm{sig}^{\sigma_0}((\boldsymbol{L}_{ll}\otimes\mathrm{I}_3)((\tilde{\boldsymbol{p}}_L-\boldsymbol{h}_L)-(1_{N_l}\otimes\boldsymbol{p}_0)))$ can achieve its convergence into a narrow neighborhood of the origin in a finite time. Furthermore, suppose $\bar{\bar{\boldsymbol{p}}}_L = (\boldsymbol{L}_{ll}\otimes\boldsymbol{I}_3)\bar{\boldsymbol{p}}_L$ and $\bar{\bar{\boldsymbol{q}}}_L = (\boldsymbol{L}_{ll}\otimes\boldsymbol{I}_3)\bar{\boldsymbol{q}}_L$. Therefore, the system can be transformed into

$$\begin{cases}\dot{\bar{\bar{\boldsymbol{p}}}}_L = \bar{\bar{\boldsymbol{q}}}_L \\ \dot{\bar{\bar{\boldsymbol{q}}}}_L = -(\boldsymbol{L}_{ll}\otimes\boldsymbol{I}_3)(l_3 sig^{\beta_1}(\bar{\bar{\boldsymbol{p}}}_L) + l_4\mathrm{sig}^{\beta_2}(\bar{\bar{\boldsymbol{q}}}_L))\end{cases}. \tag{41}$$

For the follower layer, suppose $\bar{\boldsymbol{p}}_F = \boldsymbol{p}_F - \tilde{\boldsymbol{p}}_F$, $\bar{\boldsymbol{q}}_F = \boldsymbol{q}_F - \tilde{\boldsymbol{q}}_F$, note $\bar{\boldsymbol{p}}_C = -(\boldsymbol{L}_{ff}^{-1}\boldsymbol{L}_{lf}\otimes\boldsymbol{I}_3)\bar{\boldsymbol{p}}_L$, $\bar{\boldsymbol{q}}_C = -(\boldsymbol{L}_{ff}^{-1}\boldsymbol{L}_{lf}\otimes\boldsymbol{I}_3)\bar{\boldsymbol{q}}_L$, consider Lemma 1 and the DFTE (22), and define $\bar{\boldsymbol{p}}_{Fe} = \bar{\boldsymbol{p}}_F - \bar{\boldsymbol{p}}_C$, $\bar{\boldsymbol{q}}_{Fe} = \bar{\boldsymbol{q}}_F - \bar{\boldsymbol{q}}_C$. For the further step, note $\bar{\bar{\boldsymbol{p}}}_F = (\boldsymbol{L}_{ff}\otimes\boldsymbol{I}_3)\bar{\boldsymbol{p}}_{Fe}$ and $\bar{\bar{\boldsymbol{q}}}_F = (\boldsymbol{L}_{ff}\otimes\boldsymbol{I}_3)\bar{\boldsymbol{q}}_{Fe}$, then one can render that

$$\begin{cases}\dot{\bar{\bar{\boldsymbol{p}}}}_F = \bar{\bar{\boldsymbol{q}}}_F \\ \dot{\bar{\bar{\boldsymbol{q}}}}_F = -(\boldsymbol{L}_{ff}\otimes\boldsymbol{I}_3)(l_3\mathrm{sig}^{\beta_1}(\bar{\bar{\boldsymbol{p}}}_F) + l_4\mathrm{sig}^{\beta_2}(\bar{\bar{\boldsymbol{q}}}_F)) - \\ \qquad (\boldsymbol{L}_{lf}\otimes\boldsymbol{I}_3)(l_3\mathrm{sig}^{\beta_1}(\bar{\bar{\boldsymbol{p}}}_L) + l_4\mathrm{sig}^{\beta_2}(\bar{\bar{\boldsymbol{q}}}_L))\end{cases}. \tag{42}$$

Define $\bar{\bar{\boldsymbol{p}}} = [\bar{\bar{\boldsymbol{p}}}_L, \bar{\bar{\boldsymbol{p}}}_F]^{\mathrm{T}}$ and $\bar{\bar{\boldsymbol{q}}} = [\bar{\bar{\boldsymbol{q}}}_L, \bar{\bar{\boldsymbol{q}}}_F]^{\mathrm{T}}$. Rewriting (41) and (42) into the compact format, one can obtain the following error system of the UAV swarm:

$$\begin{cases}\dot{\bar{\bar{\boldsymbol{p}}}} = \bar{\bar{\boldsymbol{q}}} \\ \dot{\bar{\bar{\boldsymbol{q}}}} = -(\boldsymbol{M}\otimes\boldsymbol{I}_3)(l_3\mathrm{sig}^{\beta_1}(\bar{\bar{\boldsymbol{p}}}) + l_4\mathrm{sig}^{\beta_2}(\bar{\bar{\boldsymbol{q}}}))\end{cases} \tag{43}$$

where $\boldsymbol{M} = \begin{bmatrix}\boldsymbol{L}_{ll} & \boldsymbol{0} \\ \boldsymbol{L}_{lf} & \boldsymbol{L}_{ff}\end{bmatrix}$, which is a positive definite matrix according to Assumption 2 and Assumption 3. Define the candidate Lyapunov function of the system (43) as follows:

$$V(\bar{\bar{\boldsymbol{p}}}, \bar{\bar{\boldsymbol{q}}}) = \sum_{i=1}^{N}\sum_{j=1}^{3}\int_0^{\bar{\bar{p}}_{ij}} l_3\mathrm{sig}^{\beta_1}(\rho)\mathrm{d}\rho + \frac{1}{2}\bar{\bar{\boldsymbol{q}}}^{\mathrm{T}}(\boldsymbol{M}^{-1}\otimes\boldsymbol{I}_3)\bar{\bar{\boldsymbol{q}}}. \tag{44}$$

The derivative of $V(\bar{\bar{\boldsymbol{p}}}, \bar{\bar{\boldsymbol{q}}})$ is obtained that

$$\dot{V}_1(\bar{\boldsymbol{p}},\bar{\boldsymbol{q}}) = l_3\sum_{i=1}^{N}\sum_{j=1}^{3}\mathrm{sig}^{\beta_1}(\bar{p}_{ij})\dot{\bar{p}}_{ij} + \bar{\boldsymbol{q}}^{\mathrm{T}}(\boldsymbol{M}^{-1}\otimes\boldsymbol{I}_3)\dot{\bar{\boldsymbol{q}}} = -l_4\left\|\bar{\boldsymbol{q}}\right\|_2^{\beta_1+1} \leqslant 0.$$

If and only if $\bar{\boldsymbol{q}} = \boldsymbol{0}$, there is $\dot{V}_1(\bar{\boldsymbol{p}},\bar{\boldsymbol{q}}) = 0$. From the LaSalle's Invariance Principle [57], it is clear that the system (42) is asymptotically stable. Besides, according to Lemma 2, the system is homogeneous of degree $\beta = (\beta_1 - 1)/2 < 0$ related to the vector $(1, (1+\beta_1)/2)$. Thus, the system globally converges to zero in a finite time. □

4. Simulations and analyses

4.1 Description of simulation scenarios

A topology $\mathcal{G}$ of the UAV swarm composing of eight leader UAVs (Numbered from 1 to 8) and four follower UAVs (Numbered from 9 to 12) are shown in Fig. 4. It can be proved that the topology is satisfied with Assumption 2 and Assumption 3. The model parameters of each UAV are shown in Table 2. Also, consider that the real input has saturation limits with $0\,\mathrm{N} \leqslant T_i \leqslant 25\,\mathrm{N}$, $-12^\circ \leqslant \alpha_i \leqslant 12^\circ$, and $-60^\circ \leqslant \phi_i \leqslant 60^\circ$.

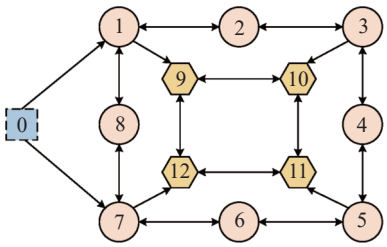

Fig. 4 Topology of the UAV swarm

Table 2 Model parameters of each UAV

Parameter	Value
m/kg	1.5
g/ (m·s^{-2})	9.81
ρ/(kg·m^{-3})	1.225
C_{D0}	0.05
C_{L0}	0.06
C_L^{α}/(°)	0.4
S/m^2	0.06
l_b/m	0.6
l_c/m	0.15

At the initial time the scalar velocity V_i of each UAV is 20 m/s, and the path angle $\theta_i(0)$ and the heading angle $\psi_i(0)$ are all zero. The initial positions of UAVs are randomly generated, chosen as: $\boldsymbol{p}_1(0)$ = [−151 m,11 m, 1 747 m]$^{\mathrm{T}}$, $\boldsymbol{p}_2(0)$ = [−1 271 m,11 m,1 677 m]$^{\mathrm{T}}$, $\boldsymbol{p}_3(0)$ = [−1 216 m,24 m,830 m]$^{\mathrm{T}}$, $\boldsymbol{p}_4(0)$ = [−509 m,27 m,957 m]$^{\mathrm{T}}$, $\boldsymbol{p}_5(0)$ = [−371 m,24 m,1 485 m]$^{\mathrm{T}}$, $\boldsymbol{p}_6(0)$ = [−920 m,29 m, 1 482 m]$^{\mathrm{T}}$, $\boldsymbol{p}_7(0)$ = [−1 148 m,29 m,865 m]$^{\mathrm{T}}$, $\boldsymbol{p}_8(0)$ = [−478 m,30 m,1 184 m]$^{\mathrm{T}}$, $\boldsymbol{p}_9(0)$ = [−915 m,23 m, 1 329 m]$^{\mathrm{T}}$, $\boldsymbol{p}_{10}(0)$ = [−528 m,11 m,1 141 m]$^{\mathrm{T}}$, $\boldsymbol{p}_{11}(0)$ = [−628 m,22 m,1 498 m]$^{\mathrm{T}}$, and $\boldsymbol{p}_{12}(0)$ = [−923 m,17 m, 1 359 m]$^{\mathrm{T}}$. The mean wind speed V_m at the altitude of 80 m is 4 m/s.

The disturbance input of each UAV caused by model uncertainties are chosen as $d_{w,xi} = 0.1\cos(0.1\pi t + (i-1)\pi/6)\cdot g$, $d_{w,yi} = 0.15\cos(0.1\pi t + (i-1)\,\pi/6)\cdot g$, and $d_{w,zi} = 0.15\sin(0.1\pi t + (i-1)\,\pi/6)\cdot g$. Select the lower boundaries of the execution effectiveness $\underline{\eta}_{a,i1} = 0.7$, $\underline{\eta}_{a,i2} = 0.75$, $\underline{\eta}_{a,i3} = 0.75$, and the lower boundaries of the measurement effectiveness $\underline{\eta}_{m,i1} = 0.8$, $\underline{\eta}_{m,i2} = 0.8$, respectively. By recalling the fault models (6) and (7), the actuator and sensor fault signals are shown in Table 3.

Table 3 Fault signals encountered by each fixed-wing UAV (°)

Fault component	Fault signal	$0\,\mathrm{s} < t < 60\,\mathrm{s}$	$60\,\mathrm{s} < t < 120\,\mathrm{s}$	$t > 120\,\mathrm{s}$
Actuator fault	$\eta_{a,i1}$	1	$0.3\mathrm{e}^{-1.5(t-60)} + 0.7$	$0.3\mathrm{e}^{-1.5(t-60)} + 0.7$
	$\eta_{a,i2}$	1	$0.25\mathrm{e}^{-1.5(t-60)} + 0.75$	$0.25\mathrm{e}^{-1.5(t-60)} + 0.75$
	$\eta_{a,i3}$	1	$0.25\mathrm{e}^{-1.5(t-60)} + 0.75$	$0.25\mathrm{e}^{-1.5(t-60)} + 0.75$
	$b_{a,i1}$	0	$-5(1-\mathrm{e}^{-1.5(t-60)})$	$-5(1-\mathrm{e}^{-1.5(t-60)})$
	$b_{a,i2}$	0	$0.5(1-\mathrm{e}^{-1.5(t-60)})$	$0.5(1-\mathrm{e}^{-1.5(t-60)})$
	$b_{a,i3}$	0	$5(1-\mathrm{e}^{-1.5(t-60)})$	$5(1-\mathrm{e}^{-1.5(t-60)})$
Sensor fault	$\eta_{m,i1}$	1	1	$0.2\mathrm{e}^{-(t-120)} + 0.8$
	$\eta_{m,i2}$	1	1	$0.2\mathrm{e}^{-(t-120)} + 0.8$
	$b_{m,i1}$	0	0	$5(1-\mathrm{e}^{-(t-120)})$
	$b_{m,i2}$	0	0	$5(1-\mathrm{e}^{-(t-120)})$

The parameters for the control scheme of each UAV are chosen that: (i) for the DFTE, $\sigma_0 = 0.5$, $m_1 = 3.5$, and $m_2 = 2.5$; (ii) for the FTESO, $\kappa = 0.5$, $k_1 = 18$, $k_2 = 108$, and $k_3 = 216$; (iii) for the NITSM, $\beta_1 = 0.6$, $\beta_2 = 2\beta_1/(\beta_1 + 1) = 0.75$, $l_3 = 0.6$, and $l_4 = 3$; (iv) for the AESTW, $\sigma_1 = 0.5$, and $\sigma_2 = 2\sigma_1 - 1 = 0.4$; (v) for the adaptive law, $l_1(0) =$

5, $w_1 = 5$, $\upsilon_1 = 2$, $\chi = 0.5$, $\varepsilon = 4 / \sigma_1 = 5.71$, and $\Delta_s = 10^{-3}$.

In the simulations, two scenarios are selected to present the effectiveness of the control scheme for tracking targets of different maneuver types, including: (i) The planar formation tracks the target in cycloid motion on the 2D ground; (ii) The cubic formation tracks the spiral climbing target in 3D space. The time-varying position and velocity of the mobile target and the desired formation function of leader UAVs under the two scenarios are shown in Table 4 respectively.

Table 4 Maneuver trajectory of the dynamic target and desired formation functions of each UAV

Scenario	Signal	Parameter	Value
Planar formation	Maneuver trajectory of the dynamic target	x_0/m	$600\sin(0.05t - \pi / 2) + 8t$
		y_0 /m	0
		z_0 /m	$600\cos(0.05t - \pi / 2) - 8t + 1\,500$
		v_{x0}/(m·s^{-1})	$30\cos(0.05t - \pi / 2) + 8$
		v_{y0}/(m·s^{-1})	0
		v_{z0} /(m·s^{-1})	$-30\sin(0.05t - \pi / 2) - 8$
	The desired formation function (For UAV 1 to UAV 8)	h_{xi} /m	$400\cos(0.02t + \pi / 2)$
		h_{yi} /m	50
		h_{zi} /m	$400\sin(0.02t + \pi / 2)$
Cubic formation	Maneuver trajectory of the dynamic target	x_0 /m	$1\,500\sin(0.02t - \pi / 6)$
		y_0/m	$50 + t$
		z_0/m	$1\,500\cos(0.02t - \pi / 6)$
		v_{x0}/(m·s^{-1})	$30\cos(0.02t - \pi / 6)$
		v_{y0}/(m·s^{-1})	1
		v_{z0}/(m·s^{-1})	$-30\sin(0.05t - \pi / 6)$
	The desired formation function (For UAV 1 to UAV 8)	h_{xi} /m	$500\cos[0.02t + (2i - 1)\pi / 4]$
		h_{yi} /m	25 (i = 1,2,3,4); −25 (i = 5,6,7,8)
		h_{zi} /m	$500\sin[0.02t + (2i - 1)\pi / 4]$

4.2 Effectiveness verification

In this subsection, the effectiveness of the proposed cooperative control scheme is first verified by simulations of the two scenarios above. The UAV trajectories of two scenarios are shown in Fig. 5.

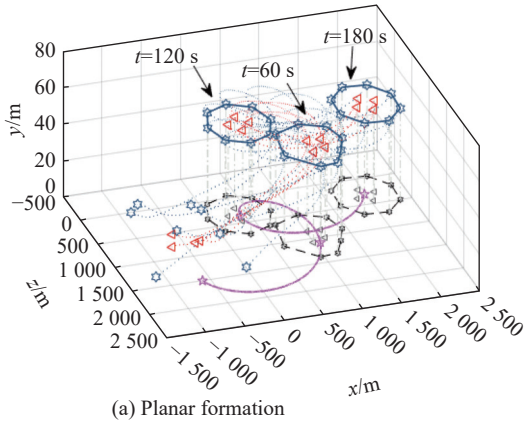

(a) Planar formation

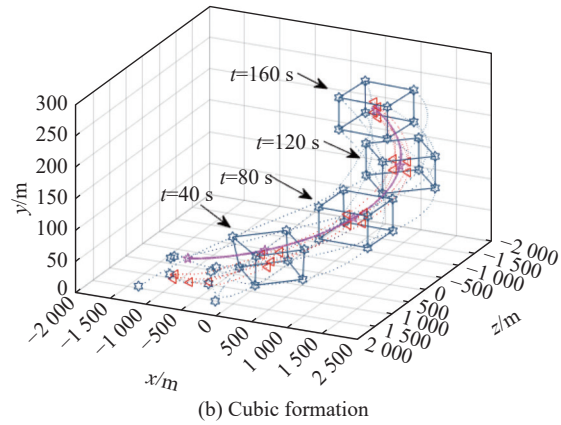

(b) Cubic formation

Fig. 5 Trajectory of each UAV in the two scenarios

In Fig. 5(a) and Fig. 5(b), the dynamic targets are marked by the purple pentagon. The black hexagrams represent the leader UAVs, while each follower is described by a red triangle. The black markers in Fig. 5(a) indicate the projection of each UAV on the ground. Apparently, whether the planar formation tracks

the target cycloidally moving on the ground or the cubic formation tracks the target spirally climbing in the 3D space, both layers of the UAV swarm can achieve the control objectives.

Without loss of generality, the following content mainly presents the simulation results and analyses of the cubic formation scenario. For the cubic formation swarm, the status of the followers and the leader at t = 40 s, 80 s, 120 s, 160 s are given. Obviously, all UAVs are scattered at the initial time, and the expected formation, containment tracking are not quite achieved at t = 40 s. Then, from t = 40 s to 80 s, all the leaders almost realize a stable time-varying cubic formation with all the followers in the convex hull all the time. After that, the states of each UAV converge further so that one can obtain higher accuracy.

As a further step, to quantitatively evaluate the effectiveness of the proposed control scheme, a dimensionless tracking error is designed as a control accuracy index. Denote the relative position tracking error and the relative velocity tracking error of UAV i as Err_{pi} and Err_{qi}, respectively, and there exist $\mathrm{Err}_{pi}=\dfrac{\|\boldsymbol{p}_i-\boldsymbol{p}_{di}\|_2}{\|\boldsymbol{p}_{di}-\boldsymbol{p}_0\|_2}$ and $\mathrm{Err}_{qi}=\dfrac{\|\boldsymbol{q}_i-\boldsymbol{q}_{di}\|_2}{\|\boldsymbol{q}_{di}-\boldsymbol{q}_0\|_2}$, where $\boldsymbol{p}_{di}$ represents the desired position and $\boldsymbol{q}_{di}$ is denoted as the desired velocity. $\|\boldsymbol{p}_i-\boldsymbol{p}_{di}\|_2$ is the absolute position tracking error, $\|\boldsymbol{q}_i-\boldsymbol{q}_{di}\|_2$ is the absolute velocity tracking error, $\|\boldsymbol{p}_{di}-\boldsymbol{p}_0\|_2$ indicates the desired distance between the dynamic target and UAV i, and $\|\boldsymbol{q}_{di}-\boldsymbol{q}_0\|_2$ interprets the error of the desired relative velocity between the dynamic target and UAV i. The position tracking error and the velocity tracking error of each UAV are depicted in Fig. 6, and it shows that the tracking error starts converging extremely small since around t = 120 s.

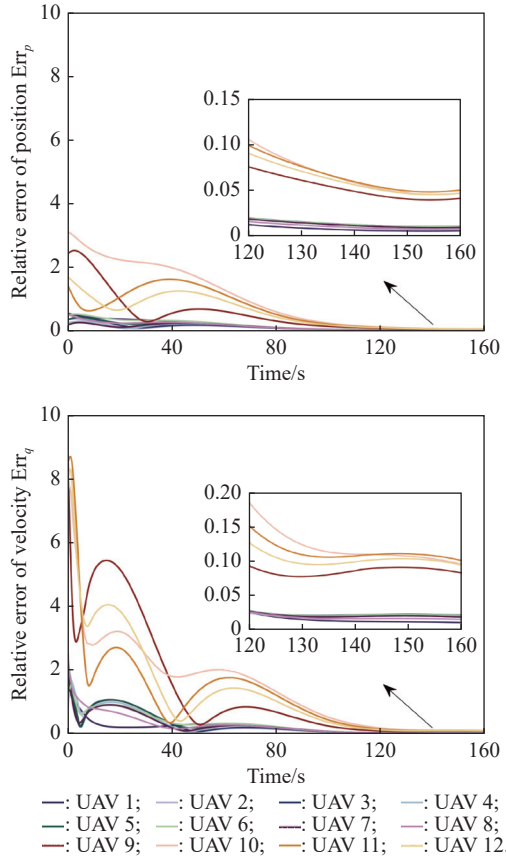

Fig. 6 Relative error of position and velocity tracking

The variation of each UAV's dynamics parameters and control inputs with time are given in Fig. 7–Fig. 9, respectively.

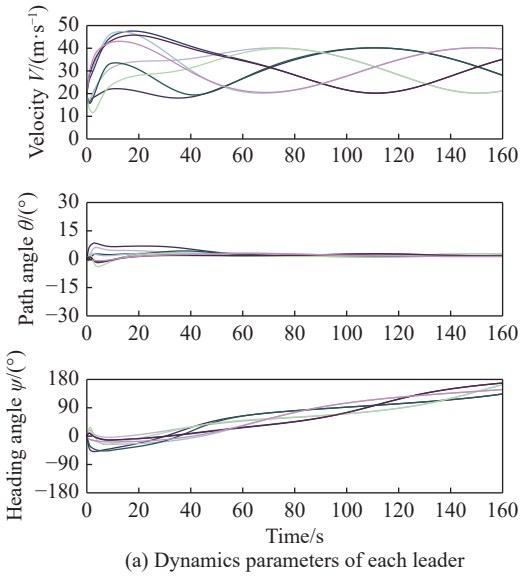

(a) Dynamics parameters of each leader

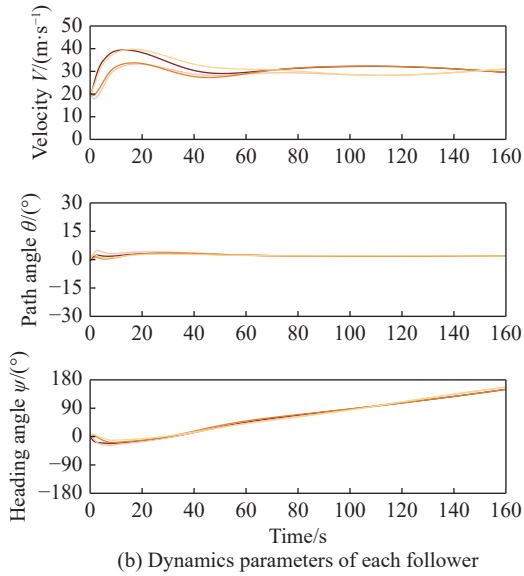

(b) Dynamics parameters of each follower

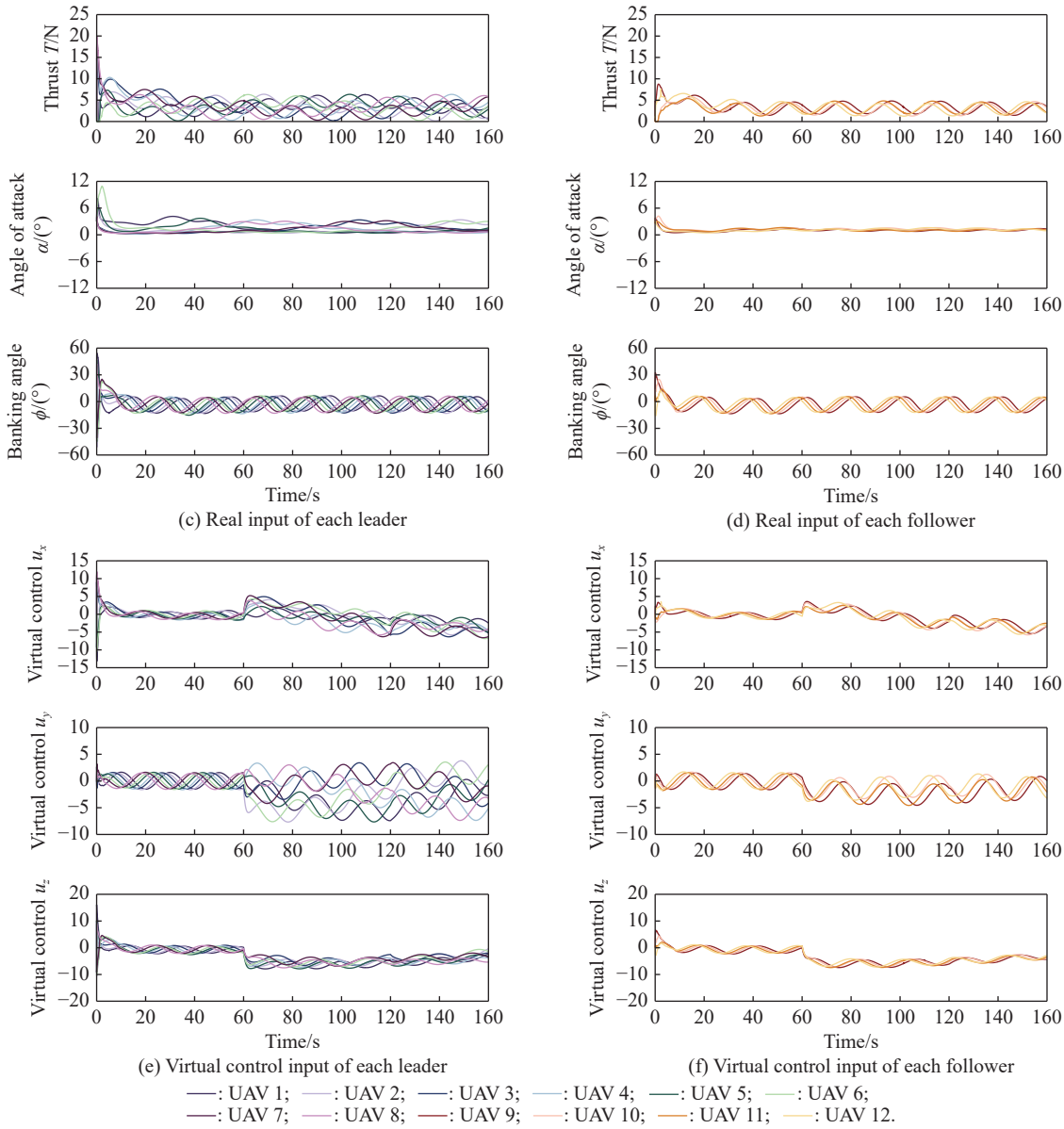

Fig. 7 Variation of dynamics parameters and control input of each UAV

It is clear that with the proposed cooperative control protocol, the fixed-wing UAV swarm is able to achieve formation, containment and tracking the dynamic target under the time-varying disturbances, actuator and sensor faults, and both layers can realize their control objectives with steady dynamic transient processes.

Further, to demonstrate the effectiveness of the proposed control protocol in diagnosing disturbances, Fig. 8 shows the disturbance observation error of FTESO for each UAV. Obviously, one can see that FTESO can achieve convergence quickly and the integrated disturbances, which are composed of model uncertainties and faults, are perfectly estimated by the FTESO.

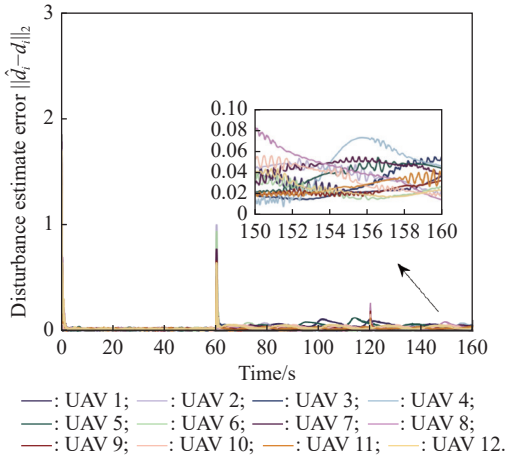

Fig. 8 Disturbance estimate error

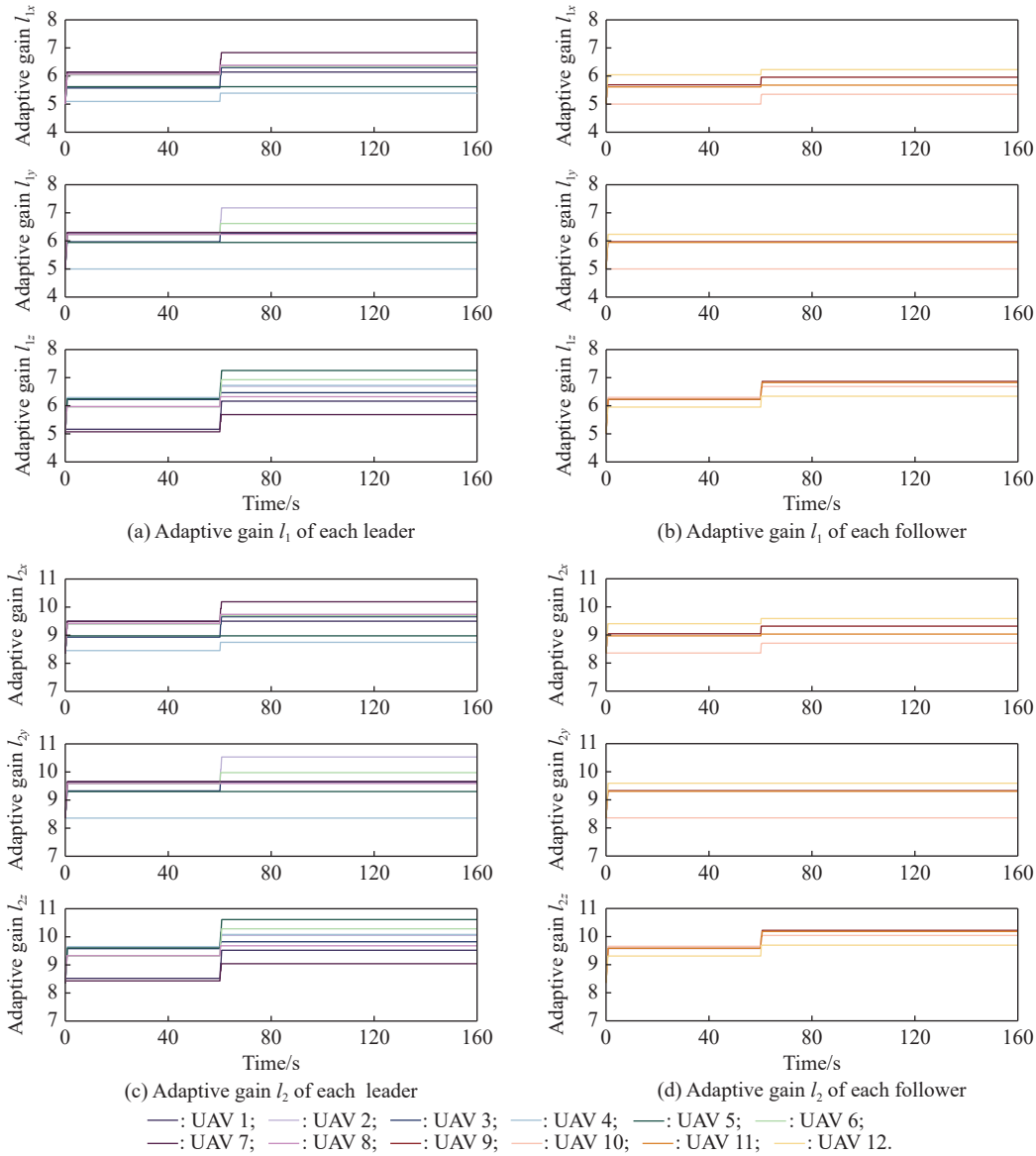

Fig. 9 Adaptive gains of AESTW for each UAV

Fig. 11 shows the convergence process of the gains of the AESTW algorithm for each UAV, which verifies the effectiveness of the adaptive law.

To further illustrate the influence of different parameters on the control performance and guide the parameter selection, the simulations for DFTE and AESTW are carried out with different parameters selecting different values. Fig. 12 and Fig. 13 show the variation of DFTE estimate error with different σ_0, m_1, m_2, and AESTW sliding modes with different σ_1, respectively.

For σ_0 in the DFTE, according to the results in Fig. 10, when σ_0 increases from 0 to 1, chattering effects will be gradually weakened and the signals vary smoothly. Nevertheless, according to Theorem 1 and Theorem 2, as σ_0 approaches 1, the estimate errors e_{pi}, e_{vi} caused by the desired time-varying formation function and target's unknown maneuvering will increase, making the upper boundness of the estimate errors, i.e., the trajectory estimation precision degraded. Thus, by adjusting σ_0, a trade-off between weakening chatter effects and guaranteeing the control precision and convergence time can be achieved. Based on the simulation results, when the value of σ_0 is selected in [0.25, 0.50], chattering effects can be significantly alleviated and the estimate errors can be guaranteed small at the same time.

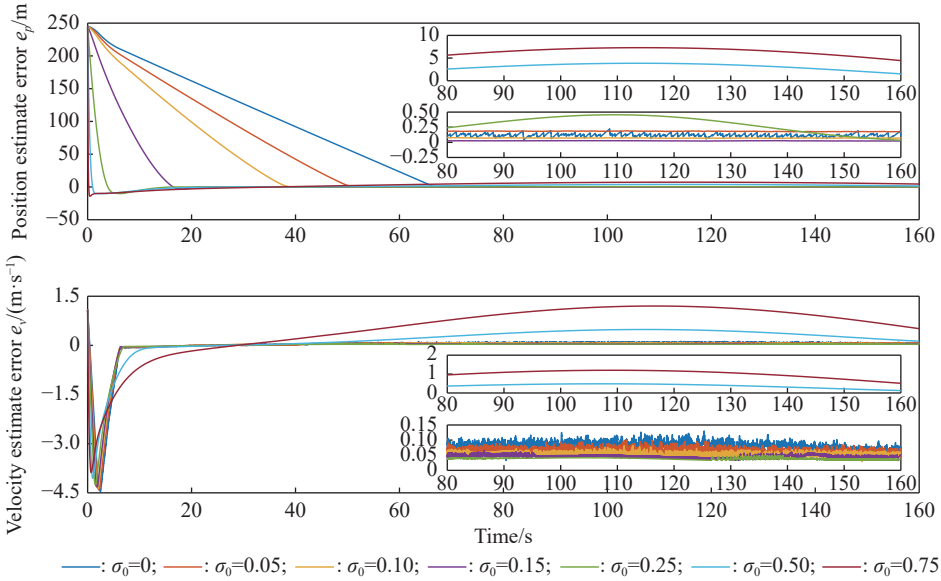

Fig. 10 Estimate error variation varying with σ_0

For $\sigma_1 \in (0.5,1), \sigma_2 = 2\sigma_1 - 1$ in the AESTW, according to the results in Fig. 11, when σ_1 increases from 0.5 to 1, chattering effects will be gradually weakened and the sliding mode variables vary smoothly. However, according to the proof and analysis in Theorem 3, when σ_1 approaches 1 (like σ_1 is selected as 0.90 or 0.95), the signal may oscillate in a small range due to the disturbance. Based on the above results, it is better to select σ_1 in [0.60, 0.80] to both weaken chattering effects and guarantee the anti-disturbance ability.

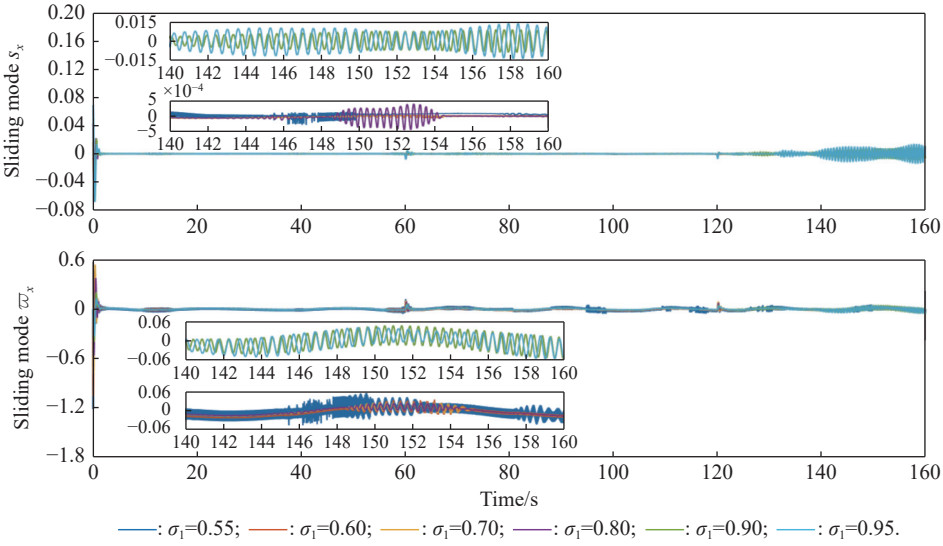

Fig. 11 UAV 1's *x*-orientation sliding mode variation varying with σ_1

To illustrate the proposed controller has anti-saturation ability, here a simulation is carried out under the actuator saturation. To show the controller performance under the saturation more clearly, here the saturation limits can be further narrowed as the 80% of the original ranges, i.e., $0\,\text{N} \leqslant T_i \leqslant 20\,\text{N}$, $-9.6^\circ \leqslant \alpha_i \leqslant 9.6^\circ$, and $-48^\circ \leqslant \phi_i \leqslant 48^\circ$. Under these real input limits, the thrust T_i, angle of attack α_i and banking angle ϕ_i in the simulation are shown in Fig. 12.

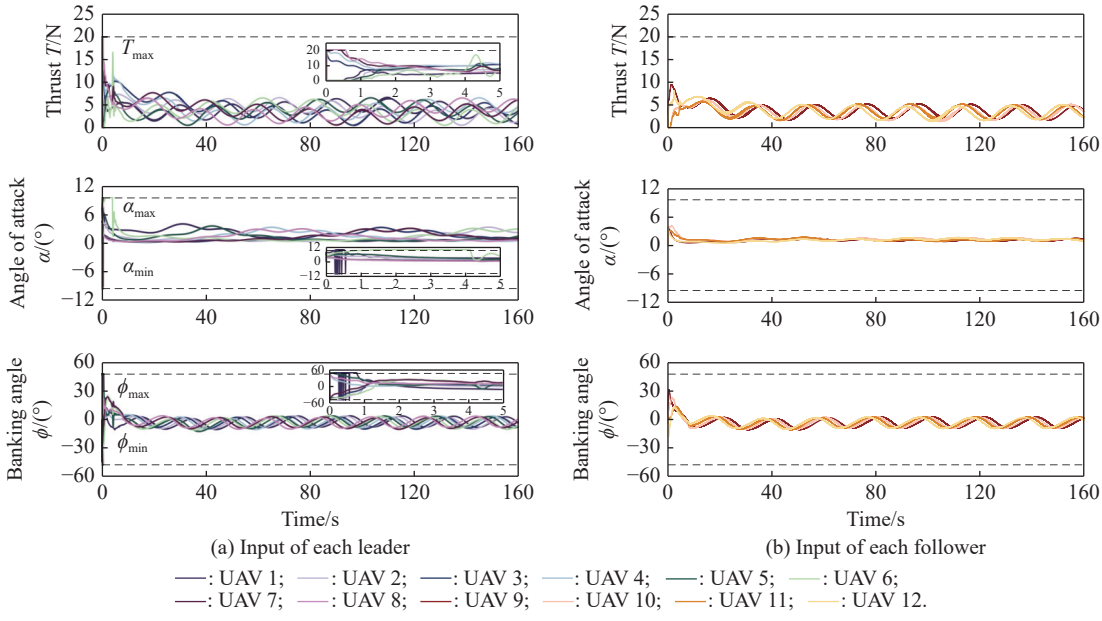

Fig. 12 Input of each UAV with saturation limits

From the simulation results, it can be seen that the thrust, angle of attack and banking angle saturation occurs at the beginning period (about 0−5 s), especially for UAV 6, of which the thrust saturation continues for about 4 s. However, the controller can still work under the control input saturation, which shows the anti-saturation ability of the designed controller.

4.3 Comparison with the existing work

In this subsection, the same problems of formation-containment control for tracking the dynamic target are also conducted by the existing distributed state estimator in [40−42] and the existing super-twisting algorithm in [43,44]. The improvements and innovations of DFTE as well as the AESTW algorithm proposed in this paper will be demonstrated by the comparisons of simulation below.

Firstly, the position estimate error e_{pi} and velocity estimate error e_{qi} of DFTE and distributed sliding-mode estimator in [40−42] are compared as are shown in Fig. 13.

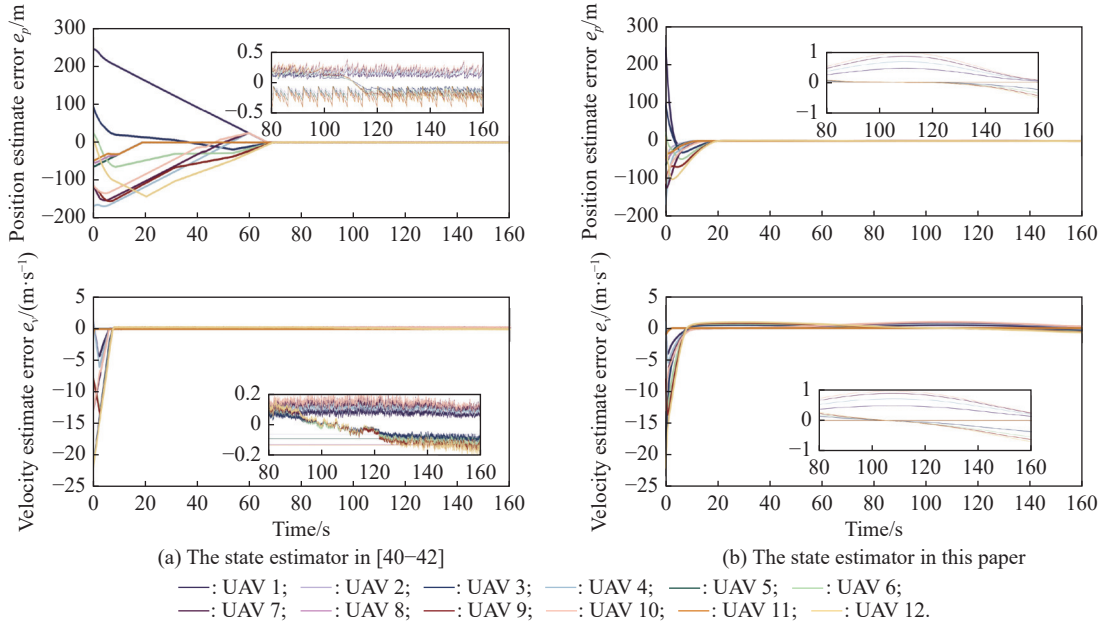

Fig. 13 Position and velocity estimate errors of the DFTE in this paper and the estimator in [40−42]

It can be seen that the distributed sliding mode-state estimator proposed in [40−42] has significant chattering effects. By the contrast, when the same gains are chosen, the proposed DFTE has a clear advantage of faster convergence, less pronounced chattering effects, and much smoother transient process.

Remark 6 Regarding the estimate error, the theoretical analysis in Theorem 1 implies that the errors of the DFTEs will converge into a small enough constant neighborhood. By selecting the control parameters, the neighborhood can be adjusted to meet the precision requirement. In that way, the proposed DFTE can achieve a compromise between the precision and the chattering effects.

As a further step, the comparative simulations are carried out with the proposed algorithm, the conventional super-twisting algorithm in [43], and the fast super-twisting algorithm in [44] to verify the superiority of the proposed AESTW algorithm. The parameters of the conventional super-twisting algorithm are chosen as $l_1 = 10$ and $l_2 = 15$, and the parameters of the fast super-twisting algorithm are selected as $l_1 = 10$, $l_2 = 15$, $l_3 = 10$, $l_4 = 15$, while the parameters of AESTW follow the previous data. Taking the x-orientation control of the leader 1, the variations of the sliding mode variables are contrasted as shown in Fig. 14.

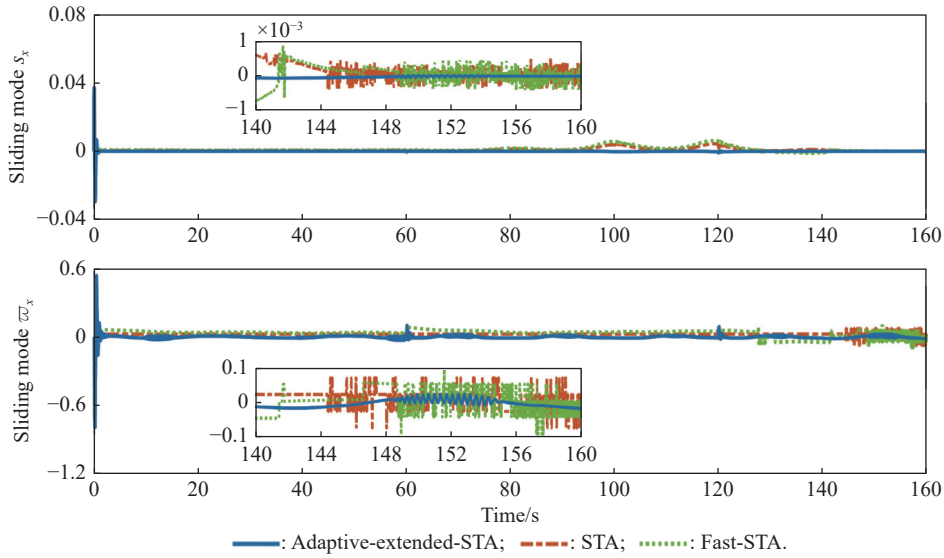

Fig. 14 Variation comparison of x-orientation sliding mode variables of UAV 1

In comparison, it is clear that the AESTW algorithm in this paper has smoother sliding mode variations and significantly weaken the chattering effects compared with the conventional super-twisting algorithm in [43] and the fast super-twisting algorithm in [44].

4.4 Robustness verification

In order to verify the robustness of the proposed controller, a Monte Carlo simulation test is conducted. Aerodynamic parameters $C_{D0}, C_{L0}, C_L^{\alpha}$ of each UAV are randomly uniformly perturbed within ±30% range.

Moreover, each UAV may encounter actuator faults and sensor faults at random instants. The efficiency losses of the thrust, angle of attack, and banking angle are randomly within 30%, 25%, and 25%. The bias of the thrust, angle of attack, and banking angle are randomly within 5 N, 2°, and 5°. A total of 500 simulations are conducted together. The results are shown in Fig. 15, and it is obvious that the response has good consistency and the dynamic performance robustness can be realized.

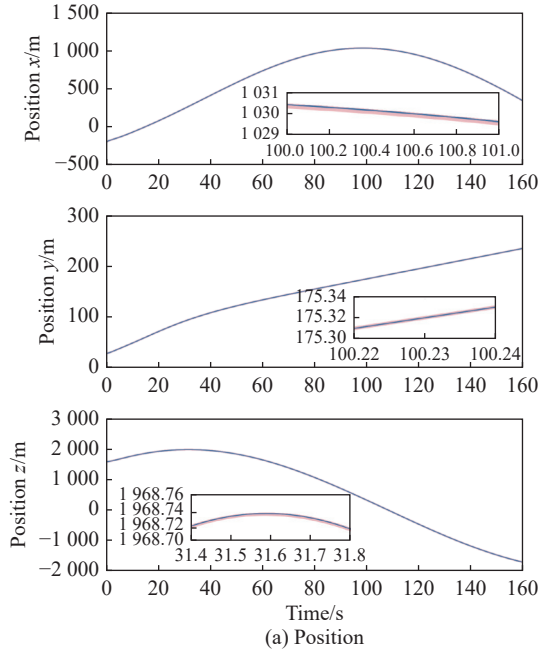

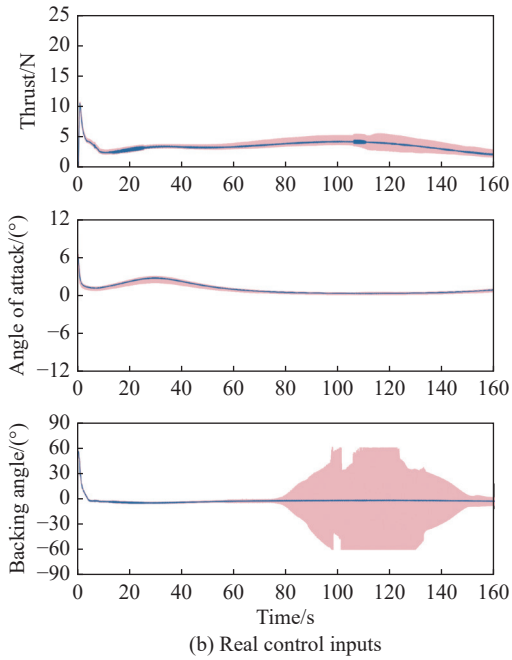

(b) Real control inputs

Fig. 15 Results of UAV 1 in 500 Monte Carlo simulations

5. Conclusions

This paper aims to present a novel two-layer distributed fault-tolerant formation-containment control scheme for "multi-leader-multi-follower" fixed-wing UAV swarm realizing formation, dynamic target tracking in 3D space under model uncertainties and actuator and sensor faults. With only a part of leader UAVs acquiring the dynamic target's states, the proposed DFTE can generate each UAV's reference trajectory which meets the control objectives in a finite-time. Compared with the previous work, the trajectories generated by DFTE vary more smoothly with less chattering effects. Further, a distributed composite FTC framework is designed to rapidly and precisely track the generated reference trajectory. The composite FTC comprises the FTESO to compensate the integrated disturbance and a novel AESTW algorithm based on integral terminal sliding modes to enhance the system robustness with less chattering effect. Stability and finite-time characteristic of the closed-loop system are proved by Lyapunov theory. Comparison simulations verify the effectiveness and competitiveness of the proposed control framework in the formation-containment control of the fixed-wing UAV swarm for dynamic target tracking under the faults and time-varying disturbances. Overall, the proposed controller possesses advantages and improvements in fault tolerance, convergence time and less chattering effect. For the research of the next step, a control scheme under the circumstance of actuator saturation and multiple environmental obstacles could be considered to further improve the controller effectiveness and system safety in more general application scenarios.

References

[1] MEI J, REN W, SONG Y D. A unified framework for adaptive leaderless consensus of uncertain multi-agent systems under directed graphs. IEEE Trans. on Automatic Control, 2021, 66(12): 6179–6186.

[2] SUN Q, CHEN J C, SHI Y. Integral-type event-triggered model predictive control of nonlinear systems with additive disturbance. IEEE Trans. on Cybernetics, 2021, 51(12): 5921–5929.

[3] RUAN Z W, YANG Q M, GE S S, et al. Adaptive fuzzy fault tolerant control of uncertain MIMO nonlinear systems with output constraints and unknown control directions. IEEE Trans. on Fuzzy Systems, 2022, 30(5): 1224–1238.

[4] XU Y, LUO D L, LI D Y, et al. Target-enclosing affine formation control of two-layer networked spacecraft with collision avoidance. Chinese Journal of Aeronautics, 2019, 32(12): 2679–2693.

[5] LIN W. Distributed UAV formation control using differential game approach. Aerospace Science and Technology, 2014, 35: 54–62.

[6] WANG J A, XIN M. Integrated optimal formation control of multiple unmanned aerial vehicles. IEEE Trans. on Control Systems Technology, 2013, 21(5): 1731–1744.

[7] XU Y, LUO D L, YOU Y C, et al. New advances in multiple autonomous aerial robots formation control technology. Science China-Technological Sciences, 2019, 62(10): 1871–1872.

[8] ZHANG Q R, LIU H H T. Robust nonlinear close formation control of multiple fixed-wing aircraft. Journal of Guidance, Control, and Dynamics, 2021, 44(3): 572–586.

[9] XU Y, LI D, LUO D L, et al. Two-layer distributed hybrid affine formation control of networked Euler-Lagrange systems. Journal of the Franklin Institute, 2019, 356(4): 2172–2197.

[10] LI Z K, WEN G H, DUAN Z S, et al. Designing fully distributed consensus protocols for linear multi-agent systems with directed graphs. IEEE Trans. on Automatic Control, 2015, 60(4): 1152–1157.

[11] NI J K, SHI P. Adaptive neural network fixed-time leader-follower consensus for multi-agent systems with constraints and disturbances. IEEE Trans. on Cybernetics, 2021, 51(4): 1835–1848.

[12] WANG Q, DONG X W, YU J L, et al. Predefined finite-time output containment of nonlinear multi-agent systems with leaders of unknown inputs. IEEE Trans. on Circuits Systems I-Regular Papers, 2021, 68(8): 3436–3448.

[13] WANG X K, LIU Z H, CONG Y R, et al. Miniature fixed-wing UAV swarms: review and outlook. Acta Aeronautica et Astronautica Sinica, 2020, 41(4): 23732.

[14] LIAN F, TEO R, WANG J L, et al. Distributed formation and reconfiguration control of VTOL UAVs. IEEE Trans. on Control Systems Technology, 2017, 25(1): 270–277.

[15] CAI Z H, WANG L H, ZHAO J, et al. Virtual target guidance-based distributed model predictive control for formation control of multiple UAVs. Chinese Journal of Aeronautics, 2020, 33(3): 1037–1056.

[16] ZHAO J, SUN J M, CAI Z H, et al. Distributed coordinated

control scheme of UAV swarm based on heterogeneous roles. Chinese Journal of Aeronautics, 2022, 35(1): 81–97.
[17] LUO Q N, DUAN H B. Distributed UAV flocking control based on homing pigeon hierarchical strategies. Aerospace Science and Technology, 2017, 70: 2570264.
[18] QIU H X, DUAN H B. Multiple UAV distributed close formation control based on in-flight leadership hierarchies of pigeon flocks. Aerospace Science and Technology, 2017, 70: 471–486.
[19] DONG X W, LI Q D, REN Z, et al. Formation-containment control for high-order linear time-invariant multi-agent systems with time delays. Journal of the Franklin Institute, 2015, 352(9): 3564–3584.
[20] LI C J, CHEN L M, GUO Y N, et al. Formation-containment control for networked Euler-Lagrange systems with input saturation. Nonlinear Dynamics, 2018, 91(2): 1307–1320.
[21] CHEN L M, LI C J, MEI J, et al. Adaptive cooperative formation-containment control for networked Euler-Lagrange systems without using relative velocity information. IET Control Theory and Applications, 2017, 11(9): 1450–1458.
[22] ZHAI D, AN L W, DONG J X, et al. Output feedback adaptive sensor failure compensation for a class of parametric strict feedback systems. Automatica, 2018, 97: 48–57.
[23] HU Q L, XIAO B, ZHANG Y M. Fault-tolerant attitude control for spacecraft under loss of actuator effectiveness. Journal of Guidance, Control, and Dynamics, 2011, 34(3): 927–932.
[24] YU X, LI P, ZHANG Y M. The design of fixed-time observer and finite-time fault-tolerant control for hypersonic gliding vehicles. IEEE Trans. on Industrial Electronics, 2018, 65(5): 4135–4144.
[25] MA H, LIANG H J, ZHOU Q, et al. Adaptive dynamic surface control design for uncertain nonlinear strict-feedback systems with unknown control direction and disturbances. IEEE Trans. on System, Man and Cybernetics System, 2019, 49(3): 506–515.
[26] CUI Y W, LI A J, MENG X F. A fault-tolerant control method for distributed flight control system facing wing damage. Journal of Systems Engineering and Electronics, 2021, 32(5): 1041–1052.
[27] PAN C W, LIU X, CHEN Y, et al. Finite-time fault-tolerant control of teleoperating cyber physical system against faults. Journal of Systems Engineering and Electronics, 2023, 34(2): 469–478.
[28] MALIKA S, WANG F Y, LIU Z X, et al. Distributed fuzzy fault-tolerant consensus of leader-follower multi-agent systems with mismatched uncertainties. Journal of Systems Engineering and Electronics, 2021, 32(5): 1031–1040.
[29] MAZARE M, TAGHIZADEH M, GHAF-GHANBARI P. Pitch actuator fault-tolerant control of wind turbines based on time delay control and disturbance observer. Ocean Engineering, 2021, 238: 109724.
[30] MAZARE M, TAGHIZADEH M. Uncertainty estimator-based dual layer adaptive fault-tolerant control for wind turbines. Renewable Energy, 2022, 188: 545–560.
[31] YU Z Q, ZHANG Y M, JIANG B, et al. A review on fault-tolerant cooperative control of multiple unmanned aerial vehicles. Chinese Journal of Aeronautics, 2022, 35(1): 1–18.
[32] LIU C, JIANG B, PATTON R J, et al. Integrated fault-tolerant control for close formation flight. IEEE Trans. on Aerospace Electronics and System, 2020, 56(2): 839–852.
[33] KAMEL M A, GHAMRY K A, ZHANG Y M. Real-time fault-tolerant cooperative control of multiple UAVs-UGVs in the presence of actuator faults. Journal of Intelligent & Robotic Systems, 2017, 88(2/4): 469–480.
[34] YANG H L, JIANG B, YANG H, et al. Synchronization of multiple 3-DOF helicopters under actuator faults and saturations with prescribed performance. ISA Transactions, 2018, 75: 118–126.
[35] YU Z Q, ZHANG Y M, JIANG B, et al. Decentralized fractional-order backstepping fault-tolerant control of multi-UAVs against actuator faults and wind effects. Aerospace Science and Technology, 2020, 104: 105939.
[36] YU Z Q, ZHANG Y M, JIANG B, et al. Fractional-order adaptive fault-tolerant synchronization tracking control of networked fixed-wing UAVs against actuator-sensor faults via intelligent learning mechanism. IEEE Trans. on Neural Networks and Learning Systems, 2021, 32(12): 5539–5553.
[37] YU Z Q, ZHANG Y M, JIANG B, et al. Distributed adaptive fault-tolerant close formation flight control of multiple trailing fixed-wing UAVs. ISA Transactions, 2020, 106: 181–199.
[38] YU Z Q, LIU Z X, ZHANG Y M, et al. Distributed finite-time fault-tolerant containment control for multiple unmanned aerial vehicles. IEEE Trans. on Neural Networks and Learning Systems, 2020, 31(6): 2077–2091.
[39] XIANG X B, LIU C, SU H S, et al. On decentralized adaptive full-order sliding mode control of multiple UAVs. ISA Transactions, 2017, 71: 196–205.
[40] LI D Y, ZHANG W, HE W, et al. Two-layer distributed formation-containment control of multiple Euler-Lagrange systems by output feedback. IEEE Trans. on Cybernetics, 2019, 49(2): 675–687.
[41] YU D, GE S S, LI D Y, et al. Finite-horizon robust formation-containment control of multi-agent networks with unknown dynamics. Neurocomputing, 2021, 458: 403–415.
[42] ZHENG W M, XU Y, LUO D L. Distributed hierarchical formation-containment control of multi quadrotors system. Journal of Beijing University of Aeronautics and Astronautics, 2022. DOI: 10.13700/j.bh.1001-5965.2022.0506. (in Chinese)
[43] LEVANT A. Higher-order sliding modes differentiation and output-feedback control. International Journal of Control, 2003, 76(9/10): 924–941.
[44] NAGESH I, EDWARDS C. A multivariable super-twisting sliding mode approach. Automatica, 2014, 50(3): 984–988.
[45] ANDERSON J D. Fundamentals of aerodynamics, McGraw-Hill series in aeronautical and aerospace engineering. 6th ed. New York: McGraw-Hill Education, 2017.
[46] AC 120-28D. Criteria for approval of category Ⅲ weather minima for takeoff, landing, and rollout. Washington: U. S. Department of Transportation and Federal Aviation Administration, 1999.
[47] BOSKOVIC J D, BERGSTROM S E, MEHRA R K. Robust integrated flight control design under failures, damage, and state-dependent disturbances. Journal of Guidance, Control, and Dynamics, 2005, 28(5): 902–917.
[48] ZHANG L L, YANG G H. Observer-based fuzzy adaptive sensor fault compensation for uncertain nonlinear strict-feedback systems. IEEE Trans. on Fuzzy Systems, 2018, 26(4): 2301–2310.
[49] XU B. Robust adaptive neural control of flexible hypersonic

flight vehicle with dead-zone input nonlinearity. Nonlinear Dynamics, 2015, 80(3): 1509–1520.
[50] XU Y, LUO D L, LI D Y, et al. Affine formation control for heterogeneous multi-agent systems with directed interaction networks. Neurocomputing, 2019, 330: 104–115.
[51] LI W Q, XIE L H, ZHANG J F. Containment control of leader-following multi-agent systems with Markovian switching network topologies and measurement noises. Automatica, 2015, 51: 263–267.
[52] MENG Z Y, REN W, YOU Z. Distributed finite-time attitude containment control for multiple rigid bodies. Automatica, 2010, 46(12): 2092–2099.
[53] BHAT S P, BERNSTEIN D S. Finite-time stability of continuous autonomous systems. SIAM Journal on Control Optimization, 2000, 38(3): 751–766.
[54] SUN C, HU G Q, XIE L H, et al. Robust finite-time connectivity preserving coordination of second-order multi-agent systems. Automatica, 2018, 89: 21–27.
[55] ZHANG W Q, DONG C Y, RAN M P, et al. Fully distributed time-varying formation tracking control for multiple quadrotor vehicles via finite-time convergent extended state observer. Chinese Journal of Aeronautics, 2020, 33(11): 2907–2920.
[56] HAN J Q. From PID to active disturbance rejection control. IEEE Trans. on Industrial and Electronics, 2009, 56(3): 900–906.
[57] K HASSAN K. Nonlinear systems. 3rd ed. New Jersey: Prentice Hall, 2002.

Biographies

QIN Boyu was born in 2000. He received his B.S. degree from Northwestern Polytechnical University, China in 2021. He currently pursues his Ph.D. degree at the School of Astronautics, Northwestern Polytechnical University, China. His research interests include cooperative planning, guidance and control of the intelligent flight vehicle swarm.
E-mail: byqin@mail.nwpu.edu.cn

ZHANG Dong was born in 1986. He received his Ph.D. degree from the School of Astronautics, Northwestern Polytechnical University, Xi'an, China, in 2013. He is currently an associate professor and doctoral supervisor of Northwestern Polytechnical University. He is also a visiting professor of the Key Laboratory of Complex System Control and Intelligent Collaborative Technology. His research interests include dynamic modeling and control of aerospace vehicles, high-speed aircraft swarms combat mission planning, and collaborative guidance and control.
E-mail: zhangdong@nwpu.edu.cn

TANG Shuo was born in 1963. He received his B.S., M.S., and Ph.D. degrees from Northwestern Polytechnical University, Xi'an, China, in 1982, 1985, and 1988, respectively. He is currently a professor with the School of Astronautics, Northwestern Polytechnical University, Xi'an. His current research interests include aerospace vehicle design, flight dynamics, flight simulation, and virtual prototype technology.
E-mail: stang@nwpu.edu.cn

XU Yang was born in 1987. He received his Ph.D. degree from Xiamen University, Xiamen, China, in 2019. He has been a visiting Ph.D. student at National University of Singapore from 2016 to 2018, and a research fellow at Westlake University from 2019 to 2020. Now, he is an associate professor in School of Civil Aviation, Northwestern Polytechnical University. His research interests include control theory and application of multiple robotic systems.
E-mail: yang.xu@nwpu.edu.cn